Plasmodium falciparum disruption of pericyte angiopoietin-1 secretion contributes to barrier breakdown in a 3D brain microvessel model

Pericyte dysfunction by malaria in *in vitro* microvessels

Rory K. M. Long[1,2], François Korbmacher[1], Paolo Ronchi[3], Hannah Fleckenstein[1,3], Martin Schorb[3], Waleed Mirza[1], Mireia Mallorquí[1], Ruth Aguilar[4], Gemma Moncunill[4], Yannick Schwab[3], Maria Bernabeu[1]*

[1]European Molecular Biology Laboratory (EMBL) Barcelona, Barcelona, Spain

[2]Heidelberg University, Faculty of Biosciences, Heidelberg, Germany

[3]European Molecular Biology Laboratory (EMBL), Cell Biology and Biophysics Unit, Heidelberg, Germany.

[4]Barcelona Institute for Global Health (ISGlobal), Hospital Clínic-Universitat de Barcelona, Barcelona, Spain

*To whom correspondence should be addressed. Email: maria.bernabeu@embl.es

Maria Bernabeu
EMBL Barcelona
Dr. Aiguader 88
Barcelona, Spain, 08003
maria.bernabeu@embl.es

Abstract

Disruption of the vascular protective angiopoietin-Tie axis is common in cerebral malaria (CM) patients, with elevated angiopoietin-2 (Ang-2) and reduced angiopoietin-1 (Ang-1) blood concentrations. The role of pericytes in CM pathogenesis remains unexplored, despite being a major source of brain Ang-1 secretion and evidence of pericyte damage in CM postmortem samples. Here we engineered a 3D microfluidics-based microvessel model containing both human primary brain microvascular endothelial cells and pericytes. This model replicated pericyte vessel coverage and ultrastructural interactions present in the brain microvasculature. When exposed to *P. falciparum*-iRBC egress products, 3D brain microvessels presented decreased Ang-1 secretion, increased vascular permeability, and minor ultrastructural changes in pericyte morphology. Notably, *P. falciparum*-mediated barrier disruption was partially reversed after pre-treatment with recombinant Ang-1. Our approach suggests a novel mechanistic role of pericytes in CM pathogenesis and highlights the importance of the angiopoietin-Tie axis in vascular dysfunction caused by *P. falciparum*.

Teaser

The authors reveal a role of pericytes in brain vascular dysfunction during malaria infection using bioengineered 3D models.

Introduction

Cerebral malaria (CM) is a severe neurological complication of *Plasmodium falciparum* infection, clinically characterized by coma and fatality rates averaging 15-20% (*1*). Furthermore, approximately 20% of CM survivors endure lifelong neurological sequelae such as hemiplegia, ataxia, epilepsy or speech disorders (*2*). The majority of pediatric CM-related deaths present severe brain swelling due to vasogenic edema, likely as a consequence of blood-brain barrier dysfunction (*3*). A hallmark of CM is the sequestration of *P. falciparum*-infected red blood cells (iRBC) in the brain microvasculature (*4*). While the molecular players responsible for *P. falciparum*-iRBC ligand-receptor interactions with cerebral endothelial cells have been extensively studied (*5–7*), the consequences of iRBC sequestration to the brain microvasculature require further investigation. Nevertheless, evidence suggests that the increase in vascular permeability is a result of a multifaceted process including a blockade of barrier-supportive endothelial receptors by iRBC, the release of toxic *P. falciparum* products from egressed iRBC, and a dysregulated host innate immune response (*8*, *9*).

An important pathway commonly dysregulated in CM patients is the angiopoietin-Tie axis, crucial to maintaining endothelial pro-barrier, anti-inflammatory, and anti-apoptotic functions (*10*). Binding of the vascular ligand angiopoietin-1 (Ang-1) to the endothelial receptor Tie-2 promotes vascular quiescence and the stabilization of endothelial tight junction proteins, such as Occludin and Zona Occludens-1 (ZO-1), necessary for maintaining the barrier function of the brain microvasculature (*11–13*). Conversely, angiopoietin-2 (Ang-2), which is rapidly released from small endothelial storage granules called Weibel-Palade bodies, generally acts as a Tie-2 antagonist leading to endothelial activation and vascular leakage (*14*). Given the opposing roles of these two molecules in vascular function, increased levels of Ang-2 and decreased levels of Ang-1 have been largely associated with cerebral vascular pathogenesis in a multitude of diseases (*15*, *16*). Similarly, a decrease in Ang-1, and an increase in Ang-2 and Ang-2:Ang-1 ratio has been well documented in fatal cases of both pediatric and adult CM (*17–21*). Despite its importance, the mechanisms leading to angiopoietin-Tie axis disruption in CM are poorly understood. Human pro-inflammatory cytokines and pro-coagulation proteins, such as TNF-α and thrombin, have been proposed as responsible for the increase of Ang-2 secretion by endothelial cells (*22*, *23*), but the causative agent responsible for decreased secretion of Ang-1 in CM patients remains unknown.

Smooth muscle cells and pericytes are the main cellular sources for Ang-1 secretion in the brain microvasculature (*10*). Beyond Ang-1 secretion, pericytes support the microvasculature and promote quiescence through additional roles. Structurally, pericytes wrap around cerebral

microvessels and interact with the endothelium through reciprocal ultrastructural membrane protrusions, known as peg-and-socket junctions (*24*), and secrete extracellular matrix components of the microvascular basal lamina that strengthen microvascular architecture. Functionally, pericytes regulate brain blood flow by controlling vessel diameter through constriction (*25*). Cerebral pericytes have been implicated in various vascular disorders of the central nervous system. Loss of pericytes from the cerebral vasculature in ischemic stroke and Alzheimer's disease is associated with blood-brain barrier disruption, extravasation of blood components into the brain parenchyma, and neuronal loss (*26–28*). Similarly, histopathological studies in retinal samples of fatal pediatric CM cases have revealed pericyte damage in regions of *P. falciparum*-iRBC sequestration, suggesting a similar role of these cell types in severe malaria infections (*29*). Yet, the role of cerebral pericytes in CM pathogenesis and in the dysregulation of the angiopoietin-Tie pathway remains largely unknown.

Bioengineered vascular models are emerging as powerful tools to study disease mechanisms *in vitro.* They have been successfully used to recapitulate many aspects of *in vivo* vascular disease including dysfunction of the angiopoietin-Tie pathway (*30*), and more recently, malaria pathogenesis, by modeling ligand-receptor interaction of *P. falciparum*-iRBC in microvessels (*31*) or transcriptional changes on endothelial cells upon exposure to *P. falciparum*-iRBC (*32*). Here, we have further developed our existent 3D brain microvascular model (*31*), with the addition of pericytes to create a device that recapitulates *in vivo* interactions between both cell types. We have used this advanced model to understand the molecular basis of angiopoietin-Tie dysregulation in CM. Our results indicate that *P. falciparum*-iRBC and products released during parasite blood stage egress play a role in angiopoietin-Tie dysregulation, and propose brain pericytes as a new player in CM pathogenesis.

Results

In vitro 3D brain microvessel model recapitulates *in vivo* cerebral endothelial-pericyte interactions

To investigate the role of cerebral pericytes in *P. falciparum*-mediated vascular pathogenesis, we have generated a 3D brain microvessel model that recapitulates the degree of pericyte coverage of the endothelium present in the brain microvasculature. The device is fabricated in a collagen type I hydrogel containing a microfluidic network with a pre-defined geometry, which is connected to both an inlet and outlet, enabling vessel perfusion (*33*). Previous incorporation of pericytes in similar bioengineered 3D models involved cellular addition into the collagen hydrogel itself.

112 However, this resulted in sparse interaction of pericytes with the endothelial microvessels (*33*).
113 Indeed, cerebral pericytes have been shown to cover approximately one third of the brain
114 microvasculature, albeit with slight variations along the brain vascular hierarchical network (*34*,
115 *35*). In this model, primary human brain vascular pericytes (HBVP) were seeded directly into the
116 channels along with primary human brain microvascular endothelial cells (HBMEC) at a 5:1
117 endothelial to pericyte ratio (Fig. 1A). After 3 days in culture, the two cell types appear to
118 reorganize into two different layers with luminal endothelial cells and mCherry-expressing
119 pericytes wrapping around the endothelial cells (Fig. 1B). Pericytes distributed homogenously
120 around the vessel cross-section, with approximately a third of the microvessel surface area covered
121 by pericytes (29.6% of the bottom surface and 27.3% of the top surface) (Fig. 1C). Notably,
122 endothelial VE-cadherin junctional labeling is continuous along the vessel luminal surface,
123 suggesting that pericyte presence does not disrupt the endothelial layer (Fig. 1D). Furthermore,
124 endothelial cells in the microvessel network express other common endothelial adherens and tight
125 junction markers, such as β-catenin and ZO-1 respectively (Fig. 1E). Labeling by α-smooth muscle
126 actin (αSMA) shows that pericytes appear as elongated cells with thin processes stretching over
127 multiple endothelial cells, and located abluminally between the endothelial layer and the collagen
128 hydrogel, as suggested by an orthogonal view (Fig. 1D). Pericyte cellular identity was confirmed
129 by the expression of a combination of cerebral pericyte cellular markers including αSMA (Fig. 1D),
130 platelet derived growth factor receptor β (PDGFRβ) and nerve/glial antigen 2 (NG-2) (Fig. 1E) (*36*,
131 *37*). Importantly, labeling of cerebral pericytes colocalized with laminin and collagen IV staining,
132 suggesting that pericytes contribute to the secretion of extracellular matrix components that
133 compose the basal lamina *in vivo* (Fig. 1E) (*38*).

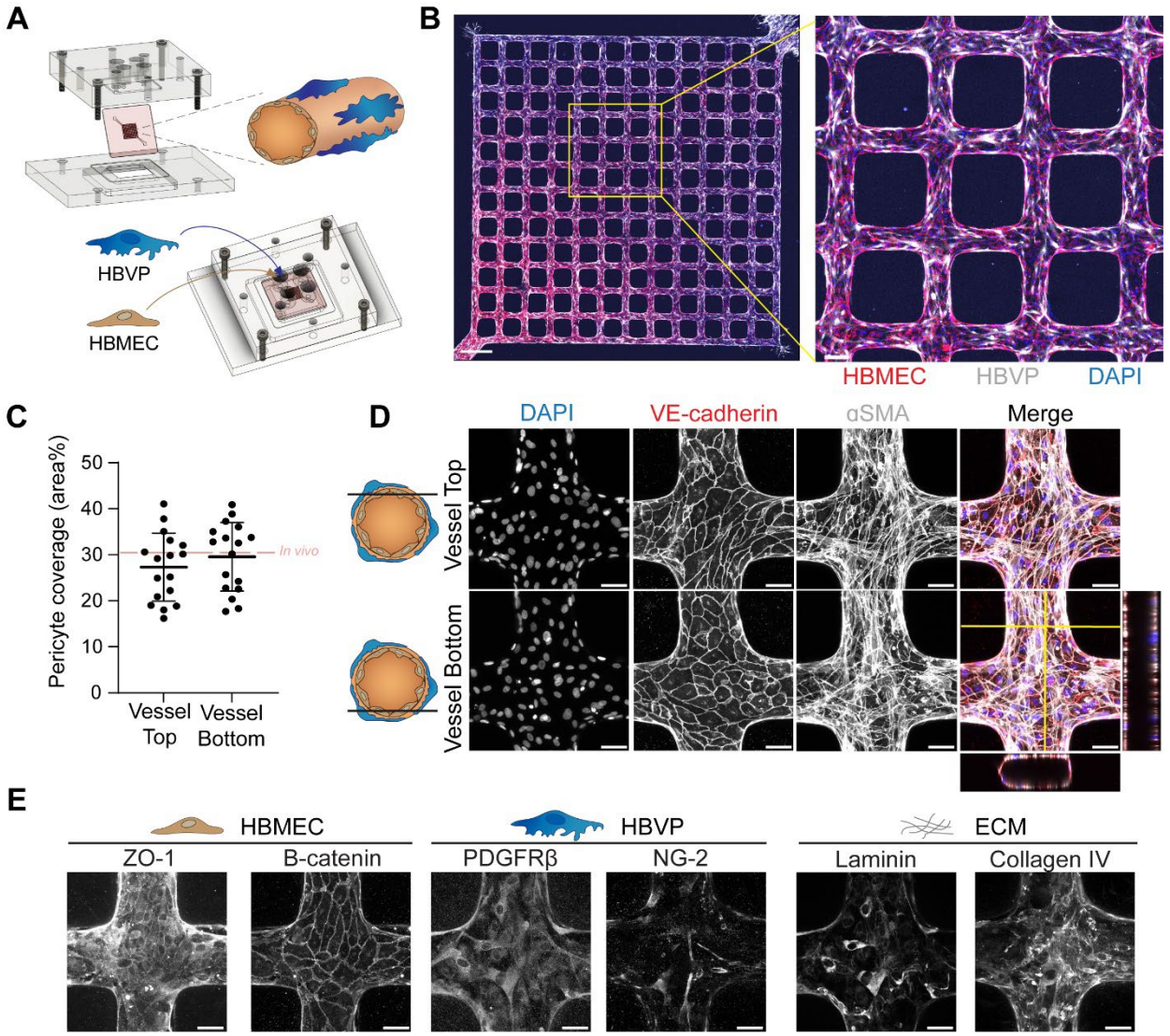

Fig. 1. A microfluidics-based 3D brain microvessel model recapitulates *in vivo* brain vascular architecture and pericyte coverage. (**A**) Schematic depiction of the fabrication pieces and device set-up (top-left), including a representation of resultant endothelial-pericyte interactions (top-right). Schematic depiction of the seeding method used to generate the 3D microvessel model (bottom). (**B**) Immunofluorescence assay (IFA) maximum z-projection of the full network of cellularized channels labeled with Von-Willebrand factor for HBMEC (red), mCherry expressing HBVP (white) and DAPI (blue) (left). Inset highlighting pericyte coverage of the microvessels (right). Scale bars represent 500 µm and 100 µm (Inset). (**C**) Quantification of the percentage of endothelial microvessel area covered by pericytes on either the top or bottom microvessel surface in a z cross-sectional view. Red dashed line represents estimated *in vivo* brain microvascular pericyte coverage. Data points represent quantification of 17 devices with statistical analysis determined by Mann-Whitney U test. Error bars represent mean +/- standard deviation. (**D**) IFA maximum z-projection of VE-cadherin, αSMA, and DAPI labeling on the top and bottom cross-sectional surfaces of microvessels (left). Merge and orthogonal view with VE-cadherin (red), αSMA (white) and DAPI (blue) (right). (**E**) IFA maximum z-projection of brain endothelial markers, ZO-1 and β-catenin, brain pericyte markers, NG-2 and PDGFRβ, and extracellular matrix markers, laminin and collagen IV. Scale bars represent 50 µm in D and E.

152 Volumetric electron microscopy has been previously used to characterize *in vivo* 3D ultrastructural
153 interactions between pericytes and endothelial cells of the cerebral microvasculature (*24*). To
154 characterize the spatial and ultrastructural organization of pericytes and endothelial cells in the
155 model, we utilized Serial Block-Face Scanning Electron Microscopy (SBF-SEM) (*39*), a volume
156 electron microscopy technique that provides nanoscale resolution of samples in a large field of view
157 (*40*). We imaged a 100 μm segment of a microvessel branch with a 15x15x50 nm xyz resolution,
158 followed by cellular segmentation and rendering. We characterized microvessel coverage of
159 approximately 25 individual pericytes, distinguished from endothelial cells by the presence of a
160 highly granulated cytoplasm (*41*). Cross-sectional analysis and segmentation of the microvessel
161 revealed an ovoid microvessel morphology, and confirmed the presence of pericytes at the
162 abluminal side of the endothelial cells (Fig. 2A). Pericytes acquired a classical bump-on-a-log
163 morphology, with the soma being the thickest region of the cell, and their longitudinal axis aligned
164 with the direction of flow (Fig. 2B). Most of the endothelial-pericyte interface is composed of thin
165 pericytic lamellae (100-300 nm thickness) that cover large areas of the endothelial surface, with
166 multiple thin pericytic branches appearing mostly at the cell periphery, as described previously
167 (*24*). A close up of regions of pericyte-endothelial cell interaction reveal that the membranes of
168 both cell types are in close proximity, even though peg-and-socket junctions were not found (Fig.
169 2C). Although pericytes constitute a heterogenous cell population depending on their location
170 within the vascular branch, their morphology in the model, coverage of endothelial cells, and co-
171 staining of αSMA, PDGFRβ and NG-2 (Fig. 1D-E) are reminiscent of ensheathing pericytes
172 commonly found in arterioles (*42*, *43*). Overall, the 3D *in vitro* brain microvessel model
173 recapitulates *in vivo* interactions between cerebral endothelial cells and pericytes, both at the tissue
174 and ultrastructural level, that can next be utilized to model the role of pericytes in malaria
175 pathogenesis.

176

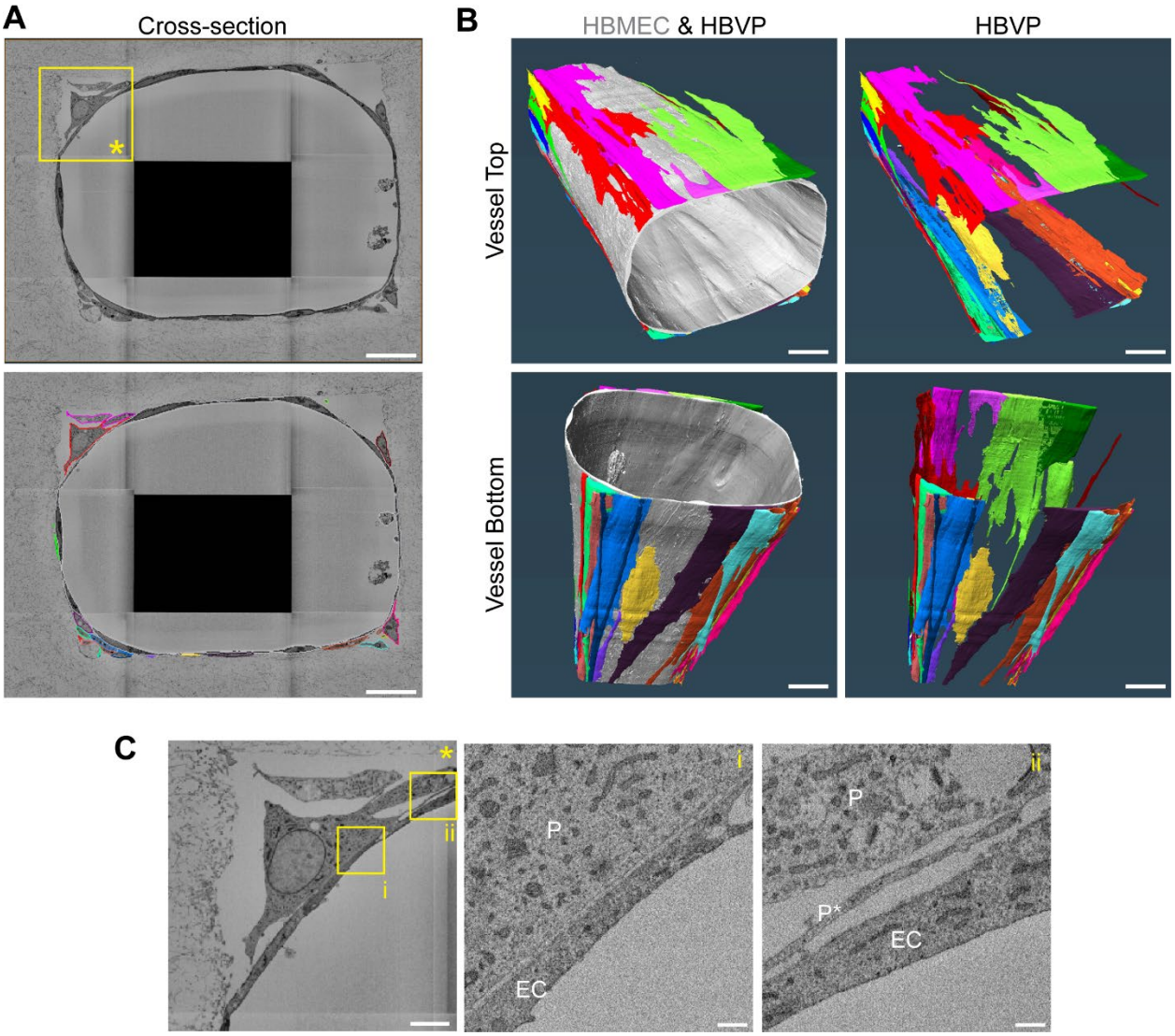

Fig. 2. Serial Block-Face Scanning Electron Microscopy reveals ultrastructural interactions between pericytes and endothelial cells. (**A**) A cross-section of the microvessel imaged through the SBF-SEM volume (top) and the corresponding segmentation outlines of the endothelium (grey) and surrounding pericytes (coloured). Scale bars represent 20 µm. (**B**) 3D rendering of the segmented microvessel (grey) and the surrounding pericytes viewed from above or below. Scale bars represent 10 µm. (**C**) Zoomed images of the ROI in A. Insets show ROIs i and ii where pericytes are denoted with "P", endothelial cells by "EC" and pericyte lamellae by "P*". Scale bars represent 5 µm (left) and 500 nm in the insets (center and right).

188 ***P. falciparum* egress products increase vessel permeability but only cause minor changes in**
189 **pericyte morphology**

190 Multiple *in vitro* studies have shown that *P. falciparum* products released during malaria parasite
191 egress disrupt the endothelial barrier (*44–48*). To characterize the impact that these could have on
192 pericyte function, we established a protocol to create media enriched for *P. falciparum*-iRBC
193 egressed products, denoted from here on as iRBC-egress media. Briefly, tightly synchronized
194 schizont stage-iRBCs were purified and allowed to egress in vascular growth media, followed by
195 recovery of the supernatant fraction containing *P. falciparum* soluble products at an estimated
196 concentration of $5x10^7$ ruptured iRBC/mL (equivalent to simultaneous egress of approximately a
197 1% parasitemia) (fig. S1A-B). We measured the endothelial disruptive properties of iRBC-egress
198 media by the xCELLigence system, which provides real time measurement of cell barrier integrity
199 through impedance. The *P. falciparum* egress products caused a significant, dose-dependent
200 decrease in cell index, a measurement of monolayer barrier function normalized to untreated cells,
201 that reached a maximum disruption at 18 hours (fig. S1C). To elucidate if iRBC-egress media also
202 induces barrier breakdown in the brain 3D microvessel model, we performed permeability assays
203 in a simpler microvessel network which consists of a single 200 µm channel. After perfusion and
204 incubation with iRBC-egress media for 18 hours, *P. falciparum* egress products accumulated on
205 the lateral and bottom walls of the microvessel and appeared as dark spots in brightfield that were
206 DAPI-positive by confocal microscopy, suggesting the presence of hemozoin, food vacuoles and
207 parasite DNA remnants (Fig. 3A and B). Microvessels perfused with iRBC-egress media presented
208 a significant increase to 70 kDa FITC-dextran permeability across the entire vessel wall,
209 corresponding to a 6-fold increment compared to vessels perfused with vascular cell media
210 ($4.08x10^{-6}$ cm/s in media-only vs. $2.66x10^{-5}$ cm/s in devices exposed to iRBC-egress media) (Fig.
211 3B and C).

212 To determine whether increased permeability was associated with physical changes in pericytes,
213 we assessed their cellular morphology in 3D microvessels exposed to iRBC-egress media for 18-
214 hours by SBF-SEM. Pericytes maintained close spatial proximity to the endothelium in the presence
215 of *P. falciparum*-iRBC ghosts, similar to control devices exposed to vascular growth media (Fig.
216 3D). To investigate potential changes in pericyte shape, we isolated and analyzed each 3D rendered
217 pericyte (Fig. 3E-F and fig S2). Cellular features such as circularity and maximum width did not
218 differ between conditions, however, iRBC-egress media treated pericytes presented fewer branches
219 suggesting a response to iRBC-egress media (Fig. 3E-F). Altogether, our results show that *P.*

falciparum egress products cause an increase in permeability of the 3D brain microvessel model, accompanied by minor changes in pericyte morphology.

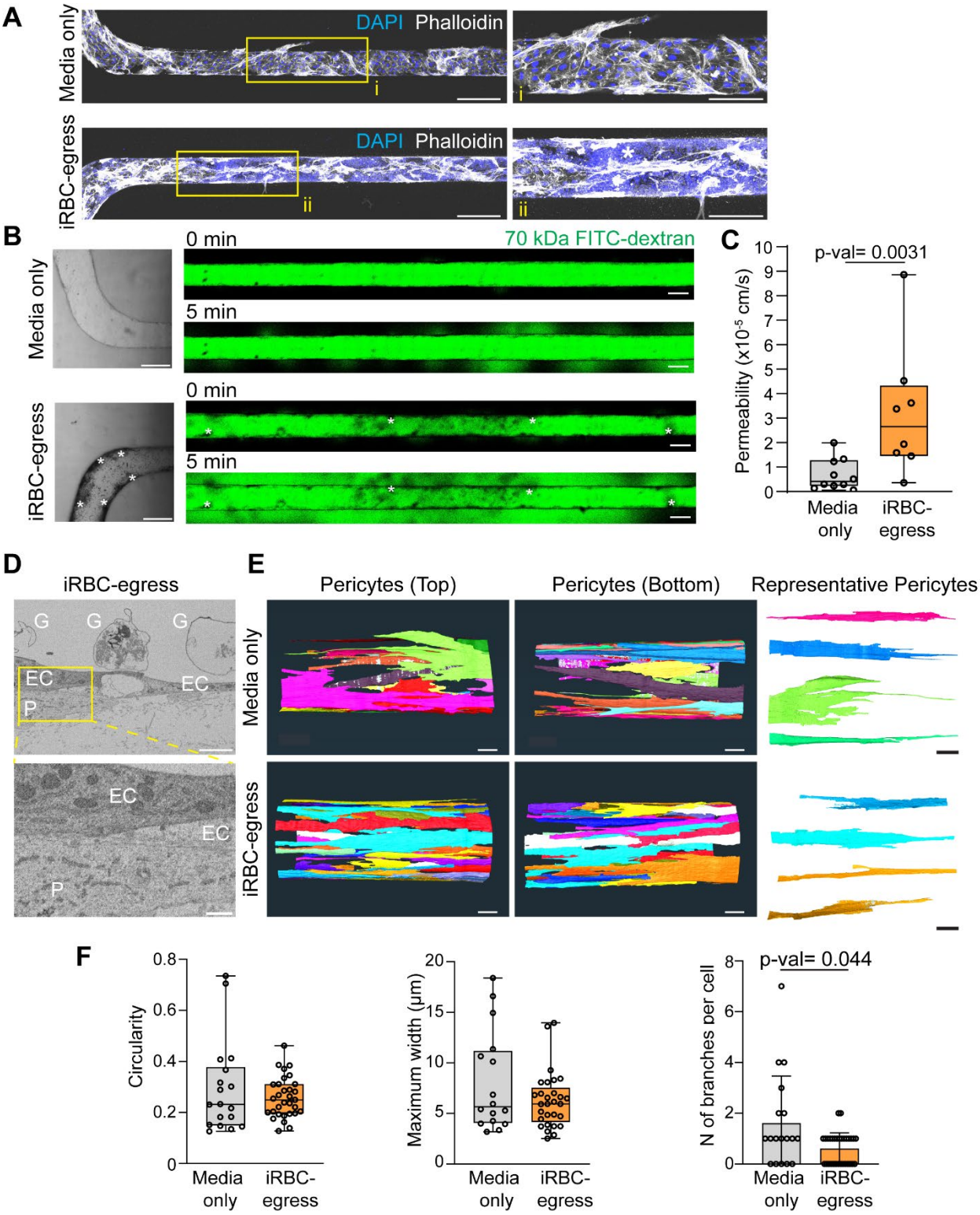

Fig. 3. iRBC-egress media increases vessel permeability and induces minor morphological changes in pericytes. (**A**) Fluorescence confocal imaging of phalloidin (white) and DAPI (blue) of single channel 3D brain microvessels treated with either media only or *P. falciparum*-iRBC-egress

media for 18-hours. Insets show ROIs of i and ii that highlight endothelial junctions and pericyte coverage (phalloidin). Accumulated DAPI-positive *P. falciparum*-iRBC egress material is denoted by an asterisk. Scale bars represent 200 µm (left) and 50 µm in inset (right). (**B**) Brightfield images near the inlet of 3D brain microvessels after 18-hour incubation with media only or iRBC-egress media (left). Representative confocal images of 70 kDa FITC-dextran flux into the surrounding collagen 0 and 5 minutes after perfusion (right). Accumulated *P. falciparum*-iRBC egress material is represented with asterisks. Scale bars represents 200 µm. (**C**) Apparent permeability of 70 kDa FITC-dextran in channels treated with media only or *P. falciparum*-iRBC egress media for 18-hours. Data points represent 8 individual devices. (**D**) SBF-SEM image and zoomed ROI of microvessels treated with iRBC-egress media. Pericytes are denoted as "P", endothelial cells by "EC" and iRBC ghosts by "G". Scale bar represents 2 µm (top) and 500 nm in inset (bottom). (**E**) 3D rendering of pericytes segmented from microvessels treated with media only or iRBC-egress media and imaged with SBF-SEM (left). Representative segmented pericytes for morphology analysis (right). Scale bar represents 10 µm. (**F**) Circularity, maximum width and number (N) of branches analysis of 18 or 31 segmented pericytes treated with media only or iRBC-egress media respectively. Box and whisker plots display the median, 25th and 75th percentiles and the minimum and maximum data points, and statistical significance was measured by Mann-Whitney U test in both C and F.

***P. falciparum*-iRBCs induce dysregulation of the angiopoietin-Tie axis**

To determine whether parasite egress products are a major driver of angiopoietin-Tie axis disruption characteristic of CM (*17–20*, *49*), we used a Luminex assay to measure secreted protein concentrations in microvessel supernatants recovered after 18-hour incubation with iRBC-egress media. Remarkably, we observed a substantial decline of Ang-1 secretion by pericytes, with concentrations nearly reaching the baseline level detected in acellular vascular growth media (Fig. 4A). Consistent with recent studies on 2D HBMEC monolayers (*22*), iRBC-egress media incubation did not result in increased Ang-2 secretion. Indeed, we quantified a significant decrease in Ang-2 secretion (Fig. 4A). Despite Ang-2 decrease, a significant increase in the Ang-2:Ang-1 ratio was found, after Ang-1 and Ang-2 concentrations were subtracted against concentrations found in the acellular vascular growth media (Fig. 4*A*). Additionally, we observed a decrease in 3D microvessel secretion or shedding of other vascular factors important for endothelial-pericyte interaction, such as Neural cadherin (N-cadherin) and Tissue Inhibitor of Metalloproteinase-1 (TIMP-1) (fig. S3A). Conversely, we detected no changes in Vascular Endothelial Growth Factor (VEGF), Tie-2, Angiopoietin-like-4 (ANGPTL4), Platelet Derived Growth Factor-BB (PDGF-BB), Interleukin-8 (IL-8) or Chemokine Ligand-1 (CXCL-1) after 18-hour incubation with iRBC-egress media (fig S3A-B).

To validate whether changes in the angiopoietin-Tie axis occur physiologically following *P. falciparum* blood stage egress within the microvasculature, we perfused the 3D brain microvessels with schizont stage *P. falciparum*-iRBC for 30 minutes followed by a 10-minute wash. After an 18-

hour incubation period, supernatants were again recovered and analyzed by Luminex. Similar results were obtained, with a reduction in both Ang-1 and Ang-2 secretion and an increase in the Ang-2/Ang-1 ratio (Fig. 4B). Altogether, these results suggest that *P. falciparum*-iRBC hamper Ang-1 secretion by pericytes, revealing a previously unappreciated role of pericytes in the dysregulation of the angiopoietin-Tie axis in CM.

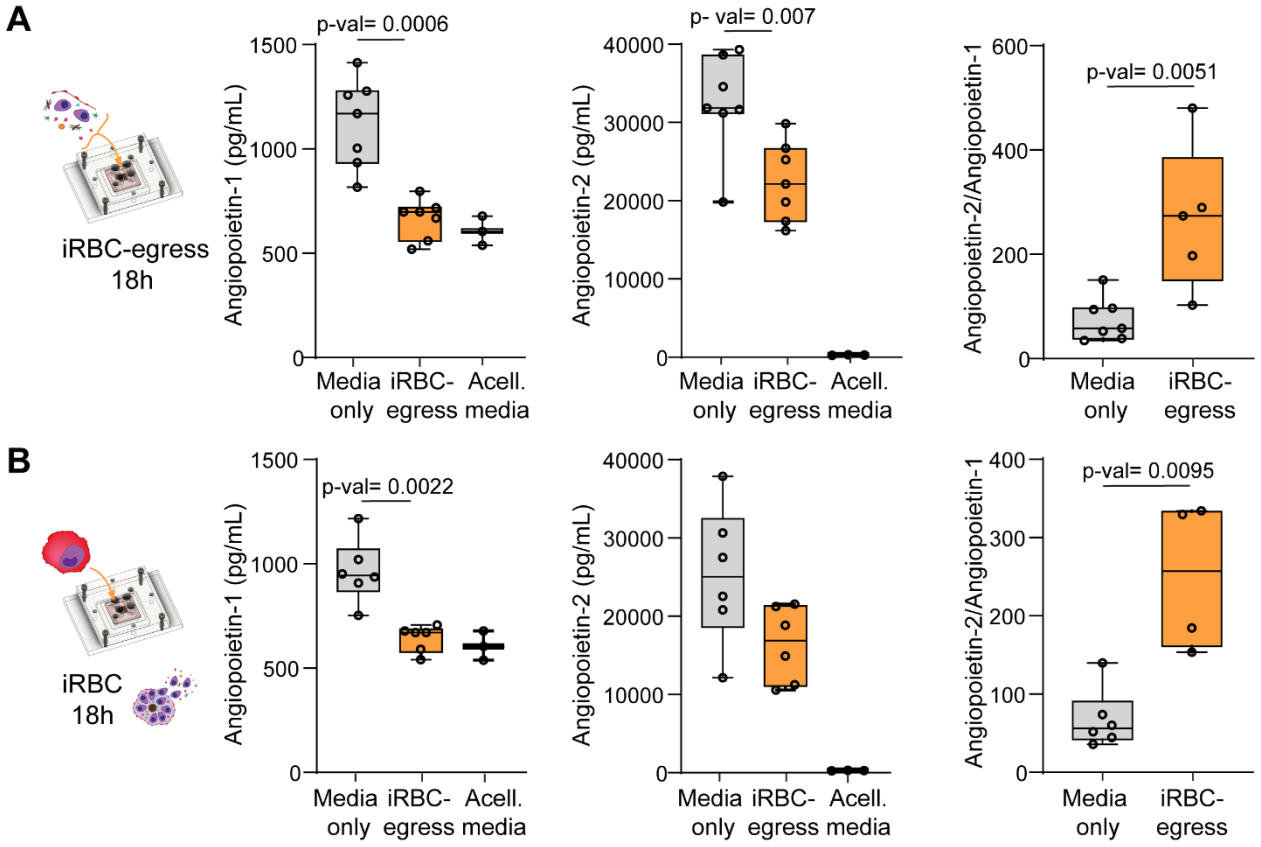

Fig. 4. *P. falciparum*-iRBC-egress media and intact *P. falciparum*-iRBC induce angiopoietin-Tie axis dysregulation. Ang-1 and Ang-2 concentrations measured in acellular media (ACell media) or 3D brain microvessels treated with media only, iRBC-egress media (**A**) or *P. falciparum*-iRBC (**B**) for 18-hours (left and center). Ang-2:Ang-1 ratio in supernatants collected from 3D brain microvessels normalized to corresponding acellular media protein concentrations (right). Box and whisker plots display the median, 25th and 75th percentiles and the minimum and maximum data points. Data points represent supernatants pooled from 2-3 devices in 6-7 independent experiments and were analyzed by Mann-Whitney U test. Acellular media measures were obtained from 3 independent aliquots. Data points in which Ang-1 concentrations measured from 3D brain microvessels were below the concentrations in acellular media were removed to calculate the Ang-2:Ang-1 ratio.

283 **Recombinant Ang-1 partially protects against endothelial barrier breakdown by iRBC-egress**
284 **media**

285 Given the key role of Ang-1 to promote vascular quiescence and endothelial barrier formation we
286 investigated whether Ang-1 supplementation could protect against the barrier disruptive effects of
287 iRBC-egress media. First, we measured barrier disruption by xCELLigence in a 2D *in vitro*
288 endothelial culture in the absence of pericytes. An 18-hour pre-treatment of recombinant Ang-1
289 (rAng-1) to resting endothelium did not change barrier properties. Conversely, an 18-hour pre-
290 treatment of rAng-1 prior endothelial cell exposure to iRBC-egress partially protected against
291 parasite-mediated endothelial barrier disruption (Fig. 5A-C). While both iRBC-egress media
292 conditions follow parallel endothelial breakdown trajectories, rAng-1 addition dampened the
293 maximum levels of disruption by iRBC-egress media, and was followed by a faster recovery to
294 endothelial monolayer baseline levels (Fig. 5B). Indeed, pre-treatment with rAng-1 conferred a
295 40% barrier breakdown protection after normalization to the untreated endothelial condition (Fig.
296 5C). Nevertheless, shorter pre-treatment periods with rAng-1 (1-hour) did not protect against iRBC-
297 egress media disruption, suggesting that the establishment of endothelial protective pathways is not
298 immediate (fig. S4).
299 Next, we tested the protective capacity of rAng-1 against iRBC-egress products in the 3D
300 microvessel model (Fig. 5D). While 3D microvessels presented a significant increase in
301 permeability values to 70 kDa FITC-dextran upon exposure to iRBC-egress media, a much smaller
302 non-significant increase was found when microvessels were pre-treated with rAng-1 for 18-hours
303 (Fig. 5E-F). Indeed, Ang-1 pre-treatment presented a 45% protection when median permeability
304 values were compared (2.66×10^{-5} cm/s in iRBC-egress media vs. 1.45×10^{-5} cm/s iRBC-egress
305 media with rAng-1 pre-treatment), similar to that seen in 2D endothelial culture. Taken together,
306 pre-treatment with rAng-1 partially protects against microvascular permeability caused by *P.*
307 *falciparum* egress products, both in 2D and 3D, highlighting the importance that a decrease in Ang-
308 1 could have in CM pathogenesis.
309

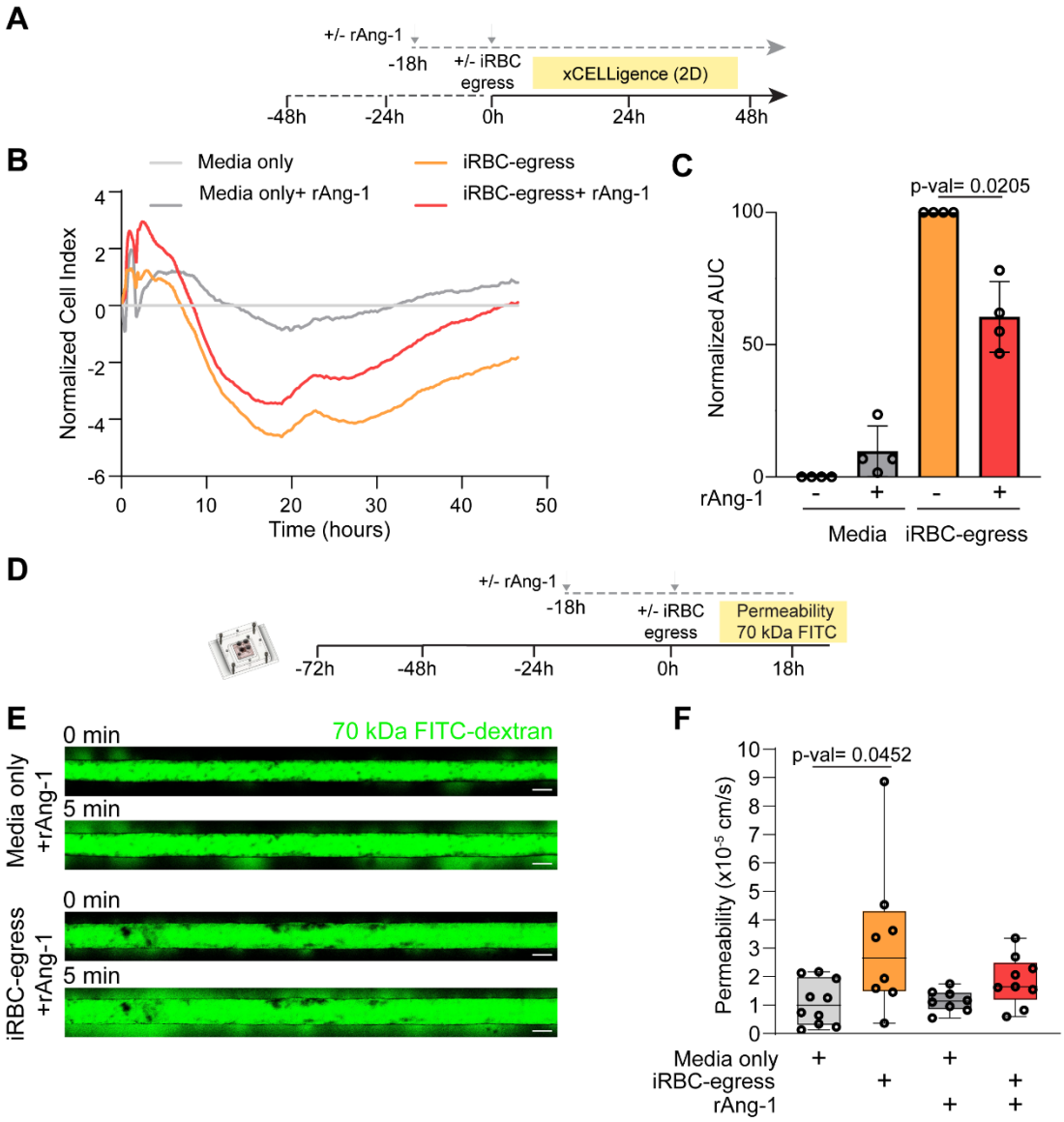

Fig. 5. Recombinant Ang-1 (rAng-1) partially protects against increased permeability induced by iRBC-egress media. (**A**) Experimental outline of the rAng-1 pre-treatment permeability experiment measured in 2D HBMEC monolayers in the absence of HBVP. (**B**) Representative recording data of xCELLigence measurements taken after an 18-hour +/- rAng-1 pre-treatment followed by +/- iRBC-egress media addition. All conditions were normalized to the media only control. (**C**) Area under the curve analysis of 4 independent experiments run in triplicate with iRBC-egress media normalized as 100. Error bars represent mean +/- standard deviation. Statistical significance is measured by repeated measures one-way ANOVA test with Dunnett's multiple comparisons test. (**D**) Experimental outline of the rAng-1 pre-treatment permeability experiment on 3D brain microvessels. (**E**) Confocal image of the 70 kDa FITC-dextran flux into the surrounding collagen at 0 and 5 minutes after dextran perfusion. Images correspond to a representative rAng-1 pretreated microvessel exposed to either media only or iRBC egress media for 18 hours. Scale bars represent 200 µm. (**F**) Apparent permeability of 70 kDa FITC-dextran in mcirovessels pretreated with or without rAng-1 followed by 18-hour media only or iRBC egress media treatment in 8-10 individual devices per condition. Box and whisker plots display the median, 25th and 75th percentiles and the minimum and maximum data points. Statistical significance was analyzed by Kruskal-Wallis test with Dunn's multiple comparisons test.

Discussion

Disruption of the angiopoietin-Tie axis is a common feature in cerebral malaria patients, often associated with disease severity and fatality (*18*, *20*). This dysregulation is also found in pediatric and adult severe malaria patients without cerebral complications (*17*, *19*) or in placental malaria (*50*). Central to this pathway are cerebral pericytes, an Ang-1 secreting cell type that is located at the interface between the vasculature and brain parenchyma, yet largely understudied in the context of cerebral malaria. Here, we developed a 3D brain microvessel microfluidic model that recapitulates the high pericyte coverage present in the brain microvasculature. Exposure of the 3D brain microvessels to *P. falciparum*-egress products caused an increase in vascular permeability accompanied by a decrease in Ang-1. Furthermore, we showed that pre-treatment with rAng-1 could, at least, partially protect against endothelial barrier breakdown. Taken together, these results suggest that the cessation of Ang-1 release upon exposure to iRBC-egress products further contributes to microvessel disruption.

The bioengineered 3D model provides important vascular mechanical cues, including estimated flow and extracellular matrix stiffnesses present in the human brain. We could reproduce the high pericyte coverage found in brain capillaries by co-seeding primary cerebral endothelial cells and pericytes through the microfluidic network. Simultaneous cell seeding, at a ratio of 5:1 (endothelial cells: pericytes), did not prevent the formation of an intact luminal endothelial monolayer that presents continuous labeling of adherens and tight junctional markers. SBF-SEM microscopy showed that both cell types sit at nanoscale distance, with the presence of thin lamellae extending from the pericyte soma covering large areas of the endothelium. Yet, despite close proximity, the recently well-described reciprocal peg-and-socket junctions were absent in the model (*24*). Overall, the 3D brain microvessel model recapitulates pericyte-endothelial interactions found in human brain vasculature making it suitable to study the role of pericytes in CM pathogenesis.

P. falciparum products released during blood stage egress have been shown to possess barrier breakdown capabilities on 2D endothelial monolayers grown on plastic. Proposed barrier disruptive *P. falciparum*-iRBC egress products include merozoite proteins, histones, heme, hemozoin and *P. falciparum* histidine rich protein 2 (*22*, *44–48*, *51*). However, their effects on pericytes remain unexplored. In this study, we confirmed that these products are disruptive in a microfluidics-based 3D brain microvessel model in the presence of pericytes. Pericytes play an important role in maintaining vascular homeostasis. For example, loss of pericytes from the cerebral vasculature leads to increased permeability in mouse models (*52*). Furthermore, dysregulation of cerebral pericytes and detachment from the vasculature have been observed in other cerebral vasculature

361 pathologies including stroke and Alzheimer's disease (*26*, *27*). In our study, we did not observe
362 gross differences on pericyte morphology or loss of vascular coverage upon treatment with iRBC-
363 egress media. Nevertheless, pericytes from iRBC-egress media-treated 3D microvessels did display
364 subtle morphological changes, having significantly less branches. The relevance of these minor
365 ultrastructural modifications in vascular barrier dysfunction could imply molecular mechanisms of
366 disease. For example, Luminex quantification upon stimulation with iRBC-egress media in the 3D
367 brain microvessel model revealed a significant reduction in N-cadherin shedding. This could point
368 towards reduced functional endothelial-pericyte interaction upon short-term incubation with *P.*
369 *falciparum*-egress products. Future studies should explore whether exposure to *P. falciparum* for
370 longer timepoints recapitulates phenotypes observed in post-mortem samples of cerebral malaria
371 patients such as vacuolization (*53*) or pericyte loss (*29*). Nevertheless, our results point towards a
372 loss of integrity at the endothelial and pericyte interface.

373 Ang-1 and Ang-2 have been considered in the past as potential biomarkers of cerebral malaria (*54*).
374 Ang-1 has excellent predictive power to distinguish malaria severity scores (*19*) or malaria from
375 other central nervous system febrile diseases (*55*). Nevertheless, the underlying mechanism of Ang-
376 1 decrease in CM remains unknown, as previous *in vitro* studies overlooked the effect that iRBCs
377 could exert on brain pericytes. To our knowledge, our study is the first one to report that *P.*
378 *falciparum* products released upon iRBC egress halt Ang-1 secretion by pericytes. A
379 complementary hypothesis for Ang-1 decrease in CM patients could be that severe
380 thrombocytopenia, commonly associated with cerebral complications in *P. falciparum* infections
381 (*7*), plays an additional role as platelets are another major source of serum Ang-1 (*56*). In light of
382 this, it is likely that both the effect of *P. falciparum*-iRBC on perivascular cells and
383 thrombocytopenia could work in concert to further contribute to a widespread decrease of Ang-1
384 levels. As for the parasite component responsible for the cessation of Ang-1 secretion, the presence
385 of accumulated light scattering, DAPI-positive iRBC-egress material suggest a role of parasitic
386 DNA or hemozoin, yet further studies are necessary to identify which iRBC-egress derived
387 component is responsible for altered signaling pathways in pericytes. Nevertheless, our results
388 highlight brain pericytes as a new player in the development of CM through dysregulation in the
389 secretion of Ang-1.

390 The use of recombinant Ang-1 as an adjunctive therapeutic against CM has long been of interest
391 (*49*) because of its role in strengthening endothelial tight junctions, as well as, upregulating anti-
392 apoptotic and anti-inflammatory pathways (*57*). Interestingly, we showed that pre-incubation of
393 human microvessels with recombinant Ang-1 partially protected against iRBC-egress mediated

394 barrier breakdown. Nevertheless, the failure to achieve complete protection upon rAng1
395 supplementation hints at the existence of other pathogenic mechanisms involved in cerebral
396 malaria-induced barrier breakdown. While the concentration of recombinant Ang-1 utilized in this
397 study was supraphysiological compared to peripheral blood samples, it is quite likely that peripheral
398 blood concentrations underestimate local concentrations at the endothelial-pericyte interface. In our
399 model, protection was only achieved after a pre-incubation of 18-hours, suggesting that downstream
400 signaling through the Tie2 receptor, such as PI3K/Akt signaling, is required (*10*). Future
401 interventions targeting the angiopoietin-Tie axis should focus on approaches that reverse
402 microvascular dysfunction after exposure to *P. falciparum.* As a proof of concept, recombinant
403 Ang-1 has previously been used as a treatment in a rodent experimental cerebral malaria model
404 after onset of disease, preserving blood-brain barrier integrity, and leading to a significantly
405 increased survival rate (*49*). Although we did not observe complete protection after short term
406 exposure, our findings point towards a mechanistic role of Ang-1 in protecting against iRBC egress-
407 mediated endothelial barrier breakdown, further highlighting Ang-1 alteration as a functional
408 contributor to CM pathogenesis.

409 Clinical studies have shown a lack of correlation between Ang-2 levels and *P. falciparum*-iRBC
410 microvascular obstruction in the rectal microvasculature (*58*) or iRBC sequestration in brain post-
411 mortem samples (*59*). Similarly, our study confirms that *P. falciparum*-iRBC sequestration in 3D
412 brain microvessel models does not directly cause Ang-2 secretion by endothelial cells. This result
413 is in concordance with a recent study that showed that Ang-2 is not secreted in response to *P.*
414 *falciparum* lysate products, but rather occurs following endothelial activation with TNF (*22*). Other
415 studies have shown Ang-2 release as a result of exposure to thrombin or hypoxia (*23*, *60*),
416 conditions that have also been associated with CM pathogenesis. Altogether, our study is in
417 agreement with previous reports suggesting that *P. falciparum* sequestration does not play a direct
418 role in the secretion of Ang-2, which instead is more likely a consequence of the activation of host
419 pro-inflammatory factors.

420 To note, our study has several limitations, including the low-throughput of the model or challenges
421 in growing the devices for long periods of time, hence preventing the modelling of long-term
422 disruptive mechanisms, such as pericyte loss. An additional limitation of our model is the absence
423 of other cells that could play an important role in maintaining the angiopoietin-Tie axis. For
424 example, Ang-1 secretion has been described in other brain and blood cell types, such as smooth
425 muscle cells (*61*, *62*), platelets and more recently, neurons and astrocytes (*63*). Yet, one of the major
426 advantages of *in vitro* bioengineered models is the opportunity to sequentially introduce different

427 components that, independently or collectively, could play a role in a complex and multifaceted
428 disease such as CM. In light of this, future iterations of the model could introduce other cell types
429 that produce Ang-1 or incorporate pro-inflammatory cytokines or thrombin, to concurrently model
430 the functional consequence of increased secretion of Ang-2 by endothelial cells.

431 In summary, our study highlights the role that pericytes could have in the development of CM
432 pathogenesis by showing for the first time that egress of *P. falciparum*-iRBC interrupt Ang-1
433 secretion by pericytes. In addition, our findings confirm that external addition of Ang-1 partially
434 protects against the increase in vascular permeability mediated by *P. falciparum* egress products,
435 providing further evidence that interventions involving the angiopoietin-Tie axis could be part of a
436 multi-targeted adjunctive therapy against CM.

437

438 **Materials and Methods**

439 **Parasite lines**:

440 HB3var03 variant *P. falciparum* parasites (dual ICAM-1 and EPCR binding), regularly panned and
441 monitored for appropriate PfEMP1 expression, were cultured in human B+ erythrocytes in RPMI
442 1640 medium (GIBCO) supplemented with 10% human type AB-positive plasma, 5mM glucose,
443 0.4 mM hypoxantine, 26.8 mM sodium bicarbonate and 1.5 g/L gentamicin. Parasites were grown
444 in sealed top T75 flasks in a gas mixture of 90% N_2, 5% CO_2 and 1% O_2. To maintain synchronous
445 cultures, parasites were synchronized twice a week in their ring stage with 5% sorbitol and once a
446 week in their trophozoite stage with 40 mg/mL gelaspan (Braun).

447 ***P. falciparum*-iRBC egress media preparation**:

448 Late-stage *P. falciparum*-iRBC (schizonts, parasitemia of 5-10%), synchronized in a 6-hour
449 window, were purified by use of 40 mg/mL gelaspan gradient separation to a final purity of >60%
450 parasitemia. The enriched *P. falciparum*-iRBC were then placed in complete RPMI media
451 containing 1 μM compound 2, a reversible PKG inhibitor that inhibits iRBC egress (kindly donated
452 by Michael Blackman, The Francis Crick Institute), at a concentration of 50 million *P. falciparum*-
453 iRBC/mL. After 5 hours, compound 2 containing media was removed and the parasites were
454 resuspended at a concentration of 100 million *P. falciparum*-iRBC/mL in vascular growth media,
455 put into a sealed top T25 flask, gassed and left in the incubator overnight on a shaker set to 50 rpm
456 to facilitate parasite egress. The resulting parasite egress efficiency was assessed by a
457 hemocytometer count and blood smear, and was then concentrated to a working concentration of
458 50 million ruptured *P. falciparum*-iRBC/mL. The resulting iRBC-egress media is spun at 1000 rpm

459 to remove cellular debris and flash frozen in liquid nitrogen until used. This concentration was
460 chosen as this value is equivalent to a circulating parasitemia of 1%, concentrations frequently
461 found in malaria patients.

462 **Primary human brain microvascular endothelial cell and primary human brain vascular**
463 **pericyte culture**:

464 Primary HBMEC (Cell Systems; ACBRI 376) were cultured according to the manufacturer's
465 recommendations in complete endothelial growth media-2MV (Lonza) containing 5% fetal bovine
466 serum. Cells were split using Trypsin/EDTA. When 90% confluent, HBMEC were seeded on 15
467 µg/mL Poly-L-lysine (P8920, Sigma) coated T75 flasks. Primary HBVP (ScienCell) were cultured
468 according to the manufacturer's recommendations in basal pericyte media supplemented with 1%
469 pericyte growth supplement, 1% penicillin/streptomycin and 2% fetal bovine serum (ScienCell).
470 Cells were split using Trypsin/EDTA when 90% confluent, seeded on 15 µg/mL Poly-L-lysine
471 coated T75 flasks, and maintained in a humidified incubator at 37 °C and 5% CO_2. All experiments
472 were conducted with HBMEC and HBVP with a passage number of 7-9.

473 **mCherry lentivirus transduction**:

474 HBVPs were grown in a T75 flask to a ~90% confluency and incubated with lentiviral particles
475 containing a mCherry vector (kindly donated by Kristina Haase Lab, EMBL Barcelona) in serum
476 free pericyte media at a multiplicity of infection of 10. After 24 hours, the lentivirus particles were
477 removed by washing once every 24-hours for a 2-day period. mCherry-positive cells were then
478 selected by fluorescence-activated cell sorting, expanded and froze down for future experiments.

479 **3D brain microvessel model fabrication**:

480 Type 1 collagen was extracted from rat tails, dissolved in 0.1% acetic acid, lyophilized in a freezer
481 dryer (Labconco Freezone 2.5 Plus) and resuspended at 15 mg/mL in 0.1% acetic acid for storage.
482 The stock collagen solution-0.1% acetic acid solution was neutralized and diluted to 7.5 mg/mL on
483 ice. A 13 by 13 channel grid or single channel pattern were negatively imprinted into the collagen
484 hydrogel by soft lithography using a PDMS stamp, and inlet and outlets were created by insertion
485 of stainless-steel dowel pins. The top pre-patterned collagen hydrogel contained in a plexiglass top
486 jig is sealed to a flat collagen-layered bottom that sits on a coverslip and a plexiglass bottom jig.
487 The assembly creates perfusable 120 µm diameter microvessels (grid design) or 200 µm diameter
488 microvessels (single channel design), as described previously (*33*, *64*). Prior to cell seeding, the
489 channels were incubated with vascular growth media, consisting in EGM-2MV (Lonza)
490 supplemented with 1x pericyte and 1x astrocyte growth factors (ScienCell) for 1 hour. Primary

491 HBMECs and HBVPs, or mCherry-positive HBVPs (for pericyte coverage analysis), were
492 resuspended at concentrations of 7 million cells/mL and mixed to a ratio of 5:1 HBMECs to HBVPs.
493 The cell mixture was then seeded into the inlet in 8 μL increments and driven through the
494 microfluidic network by gravity-driven flow. Cells were perfused twice from either the inlet or
495 outlet until the channels were completely covered with adhered cells. Media was then removed and
496 devices were flipped upside down for 1-hour to ensure even cell distribution on the top and bottom
497 of the channels. Microvessels were cultured for 3 days before being used in experiments with media
498 change every twice per day by gravity driven flow.

499 **Immunofluorescence microscopy**:

500 Microvessel labeling was performed by gravity driven flow. Microvessels were fixed with 3.7%
501 paraformaldehyde (PFA) in PBS for 15 minutes followed by three 10-minute washes with PBS.
502 Next microvessels were incubated with Background Buster (Innovex) for 30 minutes and then
503 permeabilized with blocking buffer (0.1% Triton X-100 and 2% bovine serum albumin in
504 phosphate-buffered saline (PBS)). Primary antibodies including rabbit anti-αSMA-555 (EPR5368,
505 Abcam), mouse anti-vWF (sc-365712, Santa Cruz), mouse anti-ZO-1 (Invitrogen, 10017242),
506 rabbit anti-β-catenin (Cell Signaling, 9587S), mouse anti-PDGFRβ (Abcam, ab69506), mouse anti-
507 NG-2 (Invitrogen, 10424493), rabbit anti-laminin (Abcam, ab11575), rabbit anti-collagen IV
508 (Abcam, ab6586)), mouse anti-VE-cadherin (sc-52751, Santa Cruz), and Phalloidin-647
509 (Invitrogen, A22287) were diluted in blocking buffer at 1:100 and incubated overnight at 4 °C.
510 After three 10-minute PBS washes, secondary antibodies including goat anti-mouse Alexa Fluor
511 488 (A11001, Invitrogen), goat anti-rabbit Alexa Fluor 488 (Invitrogen, A-11008), goat anti-mouse
512 Alexa Fluor 594 (Invitrogen, A-11005), goat anti-rabbit Alexa Fluor 594 (Invitrogen, A-11012),
513 goat anti-mouse Alexa Fluor 647 (A21235, Invitrogen), goat anti-rabbit Alexa Fluor 647
514 (Invitrogen, A-21244) and 2 mg/mL DAPI (D21490, Invitrogen) were diluted at 1:250 in 2% bovine
515 serum albumin and 5% goat serum containing PBS, and incubated at room temperature for 1 hour.
516 Microvessels were washed 6 times with PBS for 10 minutes each and then imaged on a Zeiss LSM
517 980 Airyscan 2. Image stacks were acquired with 3 μm or 10 μm z-step size for single or tile scan
518 images respectively. Z-projections and further threshold analysis was done using Fiji (ImageJ
519 v1.54f) software.

520 **Pericyte coverage analysis:**

521 Tile scan images of the microvessel network with mCherry-positive HBVP and vWF-labeled
522 HBMEC were acquired as described above. Images were divided into two stacks, one being the top
523 half of the microvessels of the network and the other the bottom half. Next, Z-projections of the top

524 and bottom surfaces of the network were generated. The percentage of endothelial surface that was
525 covered by pericytes was calculated by creating a mask of both the mCherry HBVP and the vWF-
526 positive HBMEC.

527 **Serial Block-Face Scanning Electron Microscopy:**

528 Microvessel devices were grown for 3 days, then treated with iRBC-egress media or vascular
529 growth media for 18hours, and then fixed by adding 2% PFA and 2.5% glutaraldehyde (GA) to the
530 device inlet for 30-minutes and washed twice with EGM-2MV at 37 °C. The collagen hydrogel was
531 then carefully removed from the plexiglass jig and microvessel regions exposed to low shear stress
532 were cut out and fixed with a secondary fixative solution (2% PFA, 2.5% GA, 0.25 mM $CaCl_2$, 0.5
533 mM MgCl, 5% sucrose in a pH 7.4 0.1 M Cacodylate buffer) overnight at 4 °C, and then rinsed
534 twice for 15-minutes with 0.1 M Cacodylate buffer. Samples were post-fixed in a reduced Osmium
535 solution (1% OsO_4, 1.5% K_3FeCN_6 in 0.065 M Cacodylate buffer) for 2-hours at 4 °C followed by
536 six 10-minute washes in dH_2O. Post-staining consisted of subsequent incubation steps of 1%
537 thiocarbohydrazide in dH_2O, 2% Osmium tetroxide in dH_2O, and 1% Uranyl acetate in dH_2O, aided
538 by a PELCO Biowave Pro+ (Ted Pella) containing a SteadyTemp Pro and ColdSpot set to 20 °C at
539 7x 2 minute cycling on-off at 100 W under vacuum, with dH_2O rinses in between steps once in a
540 fume hood and twice in the microwave at 250 W for 40 s without vacuum. The stained samples
541 were then dehydrated by serial additions of 30, 50, 80, and 100% ethanol solutions in the microwave
542 at 250 W for 40 s without vacuum with ColdSpot set to 4 °C, infiltrated with EPON 812 hard epoxy
543 resin in steps of 25, 50, 75, 90, and 3x 100% resin diluted in ethanol with each step in the microwave
544 at 150 W for 3 minutes under vacuum and polymerized at 60 °C for 48 hours. The sample was
545 trimmed (UC7, Leica Microsystems) using a 90° cryo-trimmer (Diatome) to generate a small block
546 face. The resulting resin block was mounted on a pin stub using silver conductive epoxy resin (Ted
547 Pella). The SBF-SEM acquisition was performed with a Zeiss Gemini2 equipped with a Gatan
548 3view microtome and a focal charge compensation device (Zeiss). The SEM was operated at 1.5
549 kV 300 pA, using a pixel size of 15 nm, a slice thickness of 50 nm and a dwell time of 1.6 µs. The
550 SBF-SEM acquisition was performed using the software SBEMimage (*65*). The acellular center of
551 the lumen was not imaged to save imaging time. Following acquisition, the positional metadata of
552 the sections and tiles obtained was converted with SBEM-specific import scripts
553 (https://git.embl.de/schorb/rendermodules-addons) for subsequent assembly, stitching and
554 alignment of large EM datasets (*66*). Aligned images were then binned to 22 by 22 by 250 nm^3 in
555 xyz and segmentation was then performed using the software package Amira (Thermo Fischer
556 Scientific). Primary HBVP and HBMEC were segmented semi manually using the magic wand and

557 brush tool to segment every fifth section followed by use of the interpolation tool to segment the
558 entire volume. The resulting segmented microvessels were rendered using the generate surfaces
559 module for 3D visualization.

560 ***P. falciparum*-iRBC and iRBC-egress media perfusion to 3D brain microvessels:**

561 All experiments were done in 3D microvessel devices grown for 3 days. Schizont-stage *P.*
562 *falciparum*-iRBC were purified to >60% parasitemia by 40 mg/mL gelaspan and the resulting
563 enriched population was diluted in vascular growth media to 50 million iRBC/mL (same
564 concentration as the *P. falciparum*-iRBC-egress media). 200 µL of *P. falciparum*-iRBC or *P.*
565 *falciparum*-iRBC-egress media was added into the device inlet and perfused by gravity flow for
566 30-minutes with the outlet effluent being reintroduced to the inlet every 10 minutes. Microvessels
567 treated with intact *P. falciparum*-iRBC (but not *P. falciparum*-iRBC-egress media), were then
568 washed for 10 minutes with vascular growth media. Both conditions were incubated overnight for
569 18 hours. Supernatant was then removed from the outlet and pooled for Luminex analysis, and 3D
570 brain microvessels were used for permeability studies or fixed for imaging with 3.7% PFA for 15-
571 minutes (see section immunofluorescence microscopy).

572 **Fluorescent dextran-based permeability assay:**

573 Single channel microvessel devices were grown for 3 days, then perfused and incubated for 18
574 hours with either vascular growth media or *P. falciparum*-iRBC-egress media as described above.
575 To determine resulting changes in permeability, they were perfused with a 70 kDa FITC-dextran
576 solution as follows: the device was washed 1x with PBS and placed in a Zeiss LSM 980 Airyscan2
577 confocal microscope with a temperature and CO_2 controlled imaging chamber (37 °C, 5% CO_2).
578 PBS was aspirated and 100 µL of 70 kDa FITC-dextran solution (100 µg/mL) in PBS was pulled
579 from the inlet to the outlet at 6.5 µL/min flow rate using a syringe pump (Harvard Apparatus PHD
580 2000). Tilescan confocal images of the entire channel were taken every 30 seconds for 5 minutes
581 once the channel had been filled with FITC dextran. In devices pre-treated with recombinant Ang-
582 1 (923-AB-025, R&D Systems), pre-incubation occurred at 18-hours, starting on day 2.

583 **Quantification of apparent permeability:**

584 Apparent permeability is determined as the flux of fluorescently labeled dextran across the
585 microvessel wall into the surrounding collagen hydrogel. All steps of permeability analysis were
586 performed using ImageJ. By using the following equation:

587 $$Papp = \frac{1}{I_{Vt1} - I_{Tt1}} \times \frac{I_{Tt2} - I_{Tt1}}{\Delta t} \times \frac{A_{\text{lateral tissue}}}{P}$$

588 The apparent permeability (P_{app}) was calculated using the fluorescence intensity inside the vessel
589 (I_V) and in the surrounding collagen hydrogel (I_T) at two time points t1 (0 minutes after the vessel
590 is filled with dextran) and t2 (5 minutes after the vessel is filled). Δt is the change in time, $A_{lateral\ tissue}$
591 is the area of the collagen hydrogel being examined and P is the perimeter of the microvessel.
592 To account for *P. falciparum*-iRBC-egress material that appears dark even in the presence of 70
593 kDa FITC-dextran, regions of *P. falciparum*-iRBC-egress material were excluded from the
594 calculation of the fluorescence intensity inside the vessel (I_V) by using ImageJ median smoothing
595 and the magic wand tool to select only the area of the channel without *P. falciparum*-iRBC-egress
596 material.

597 **Serial Block-Face Scanning Electron Microscopy pericyte morphology analysis:**

598 3D-rendered pericyte meshes, segmented from SBF-SEM images of microvessels treated with
599 either media alone or iRBC-egress media, were generated using Amira. Following segmentation,
600 the meshes were exported as *STL* files and processed with a custom-developed Python script,
601 designed to quantify aspects of pericyte morphology, including mesh circularity and maximum
602 width (*67*). Firstly, the 3D pericyte meshes were mapped onto a 2D plane through principal
603 component analysis (PCA), effectively reducing the data's dimensionality while retaining its most
604 significant morphological features. This mapping uses the two principal components that
605 encapsulate the dimensions with the maximum variance in the 3D mesh, thus ensuring the
606 conservation of structural information. Subsequently, convex hull analysis (*68*) was applied to
607 delineate the pericyte mesh boundaries, providing a clear representation of each structure's shape
608 by which circularity and maximum width could be measured. The circularity of each mesh is
609 calculated using the convex hull, by assessing the ratio of the area enclosed by the hull to the square
610 of the hull perimeter, with the formula for circularity given as $4\pi \times Area/Perimeter^2$. This
611 circularity metric provides insight into the roundness of the mesh, where a value closer to 1 indicates
612 a shape that is more circular, and values closer to 0 reflect more elongated or irregular shapes.
613 Additionally, the maximum width is defined by identifying the two farthest points along the convex
614 hull boundary and then calculating the greatest perpendicular distance from this line (connecting
615 the farthest points) to any point within the convex hull. This measurement represents the maximum
616 width of the pericyte mesh by assuming its length is the axis with the greater size. In addition, the
617 number of pericyte branches was calculated manually by counting the number of branches on each
618 3D rendered pericyte.

619 **Quantification of secreted proteins by Luminex Assay**:

620 Secreted protein concentrations were measured from supernatants taken from the outlets of 3D
621 brain microvessels with a 13 x 13 grid geometry. Supernatants from 2-3 devices exposed to the
622 same condition were pooled, diluted 2X and assayed using a 10-plex Human Luminex Discovery
623 Assay from R&D Systems on a Luminex 100/200. The 10-plex panel included: Ang-1, Ang-2,
624 PDGF-BB, N-cadherin, TIMP-1, ANGPTL4, VEGF, Tie-2, IL-8, and CXCL-1. Protein
625 concentrations were interpolated from a 11-point standard curve of known concentrations of
626 recombinant human proteins provided by the vendor and reported as pg/mL using xPONENT 4.2.
627 7 out of 10 analytes were in the standard curve quantification range for 100% of measurements
628 recorded, with Timp-1, N-cadherin and IL-8 having 100% of measurements above the upper limit
629 of quantification.

630 **Measuring changes in barrier integrity by xCELLigence**:

631 xCELLigence 96 well PET E-plates (300600910, Agilent) were coated with 15 μg/mL Poly-L-
632 lysine and 5000 HBMECs in 200 μL EGM-2MV were added per well. After cell adherence, the
633 plate was placed into the xCELLigence RTCA SP reader to begin baseline measurement of growth-
634 related changes in cell index (an arbitrary measure of impedance) and the cells were incubated for
635 3 days until cell index reached a plateau (indicative of cell confluence). Media was changed every
636 two days. For initial testing of the impact of iRBC-egress media on barrier integrity, on the day of
637 the experiment iRBC-egress media was added at concentrations of either 12.5, 25 or 50 million
638 ruptured iRBC/mL. Changes in cell index were measured every 15-seconds for 8 hours and then
639 every 15-minutes for 48-hours. To test the impact of Ang-1 on *P. falciparum*-iRBC-egress media
640 mediated barrier breakdown, iRBC-egress media was added at $50x10^6$ ruptured iRBC/mL after
641 either a 1- or 18-hour pre-incubation with 1 μg/mL of rAng-1. Again, changes in cell index were
642 measured every 15 seconds for 8 hours and then every 15-minutes for 48-hours. Quantification of
643 partial protection was done by first normalizing each condition to the media only control. Then the
644 area under the curve of the negative values, indicative of barrier breakdown, was calculated using
645 GraphPad Prism (version 10.0.2) where the media only without rAng-1 condition represented an
646 average value of 0 and the iRBC-egress media without rAng-1 condition an average value of 100.

647 **Statistical analysis**:

648 All statistics were obtained by use of GraphPad Prism (version 10.0.2). Non-parametric Mann-
649 Whitney U tests were performed for most experiments, except to calculate Ang-1 protection in the
650 2D xCELLigence and microvessel experiments in which a repeated measures one-way ANOVA
651 test with Dunnett's multiple comparisons test and Kruskal-Wallis test with Dunn's multiple

comparisons test were performed respectively. A P-value<0.05 was considered statistically significant.

Author contributions

R.L and M.B conceived the work. R.L, P.R, R.A, and M.B designed experiments. R.L performed most experiments with assistance of F.K, P.R, H.F, M.M, and R.A. R.L, P.R, H.F, W.M, R.A, Y.S, G.M, M.B analyzed the data. R.L and M.B wrote the original draft of the manuscript. All authors contributed to manuscript writing, revision, editing and suggestions.

Acknowledgements

We want to thank Kristina Haase (EMBL Barcelona) for her support and careful suggestions on the project and manuscript writing, as well as for assistance with the generation of mCherry HBVP with help from Violeta Beltran-Sastre. We acknowledge access to the CRG/UPF flow cytometry facility for mCherry HBVP sorting. We are grateful to Carlota Dobaño (ISGlobal) for access to the Luminex and to Michael Blackman (The Francis Crick Institute) who kindly gifted compound 2. This work was facilitated by the EMBL Electron Microscopy Core Facility (EMCF), with important assistance from Viola Oorschot on sample preparation and processing, and Karel Mocaer on image analysis. The great majority of this work was supported by the core program funding of the European Molecular Biology Laboratory (EMBL) and the European Research Council (ERC) under the European Union's Horizon 2020 research and innovation program (Grant agreement no. 948088). F.K is funded through the Marie Skłodowska-Curie grant agreement (101068552). H.F is supported by a fellowship from the EMBL Interdisciplinary (EI4POD) program under Marie Skłodowska-Curie Actions COFUND (847543). G.M. is supported by RYC 2020–029886 I/ AEI/10.13039/501100011033, co funded by European Social Fund (ESF). ISGlobal received support from the grant CEX2018-000806-S funded by MCIN/AEI/ 10.13039/501100011033, and support from the Generalitat de Catalunya through the CERCA Program. This research is part of the ISGlobal's Program on the Molecular Mechanisms of Malaria which is partially supported by the Fundación Ramón Areces.

Bibliography

1. A. M. Dondorp, C. I. Fanello, I. C. Hendriksen, E. Gomes, A. Seni, K. D. Chhaganlal, K. Bojang, R. Olaosebikan, N. Anunobi, K. Maitland, E. Kivaya, T. Agbenyega, S. B. Nguah, J. Evans, S. Gesase, C. Kahabuka, G. Mtove, B. Nadjm, J. Deen, J. Mwanga-Amumpaire, M. Nansumba, C. Karema, N. Umulisa, A. Uwimana, O. A. Mokuolu, O. T. Adedoyin, W.

684 B. Johnson, A. K. Tshefu, M. A. Onyamboko, T. Sakulthaew, W. P. Ngum, K. Silamut, K.
685 Stepniewska, C. J. Woodrow, D. Bethell, B. Wills, M. Oneko, T. E. Peto, L. von Seidlein,
686 N. P. Day, N. J. White, Artesunate versus quinine in the treatment of severe falciparum
687 malaria in African children (AQUAMAT): an open-label, randomised trial. *The Lancet*
688 **376**, 1647–1657 (2010).

689 2. G. L. Birbeck, M. E. Molyneux, P. W. Kaplan, K. B. Seydel, Y. F. Chimalizeni, K.
690 Kawaza, T. E. Taylor, Blantyre Malaria Project Epilepsy Study (BMPES) of neurological
691 outcomes in retinopathy-positive paediatric cerebral malaria survivors: a prospective cohort
692 study. *The Lancet Neurology* **9**, 1173–1181 (2010).

693 3. S. Mohanty, L. A. Benjamin, M. Majhi, P. Panda, S. Kampondeni, P. K. Sahu, A. Mohanty,
694 K. C. Mahanta, R. Pattnaik, R. R. Mohanty, S. Joshi, A. Mohanty, I. W. Turnbull, A. M.
695 Dondorp, T. E. Taylor, S. C. Wassmer, Magnetic Resonance Imaging of Cerebral Malaria
696 Patients Reveals Distinct Pathogenetic Processes in Different Parts of the Brain. *mSphere*
697 **2**, 10.1128/msphere.00193-17 (2017).

698 4. K. Dorovini-Zis, K. Schmidt, H. Huynh, W. Fu, R. O. Whitten, D. Milner, S. Kamiza, M.
699 Molyneux, T. E. Taylor, The Neuropathology of Fatal Cerebral Malaria in Malawian
700 Children. *The American Journal of Pathology* **178**, 2146–2158 (2011).

701 5. A. Kessler, S. Dankwa, M. Bernabeu, V. Harawa, S. A. Danziger, F. Duffy, S. D.
702 Kampondeni, M. J. Potchen, N. Dambrauskas, V. Vigdorovich, B. G. Oliver, S. E.
703 Hochman, W. B. Mowrey, I. J. C. MacCormick, W. L. Mandala, S. J. Rogerson, D. N.
704 Sather, J. D. Aitchison, T. E. Taylor, K. B. Seydel, J. D. Smith, K. Kim, Linking EPCR-
705 Binding PfEMP1 to Brain Swelling in Pediatric Cerebral Malaria. *Cell Host & Microbe* **22**,
706 601-614.e5 (2017).

707 6. J. Storm, J. S. Jespersen, K. B. Seydel, T. Szestak, M. Mbewe, N. V. Chisala, P. Phula, C.
708 W. Wang, T. E. Taylor, C. A. Moxon, T. Lavstsen, A. G. Craig, Cerebral malaria is
709 associated with differential cytoadherence to brain endothelial cells. *EMBO Molecular*
710 *Medicine* **11**, e9164 (2019).

711 7. P. K. Sahu, F. J. Duffy, S. Dankwa, M. Vishnyakova, M. Majhi, L. Pirpamer, V.
712 Vigdorovich, J. Bage, S. Maharana, W. Mandala, S. J. Rogerson, K. B. Seydel, T. E.
713 Taylor, K. Kim, D. N. Sather, A. Mohanty, R. R. Mohanty, A. Mohanty, R. Pattnaik, J. D.
714 Aitchison, A. Hoffmann, S. Mohanty, J. D. Smith, M. Bernabeu, S. C. Wassmer,
715 Determinants of brain swelling in pediatric and adult cerebral malaria. *JCI Insight* **6** (2022).

716 8. M. Bernabeu, J. D. Smith, EPCR and Malaria Severity: The Center of a Perfect Storm.
717 *Trends in Parasitology* **33**, 295–308 (2017).

718 9. S. C. Wassmer, T. F. de Koning-Ward, G. E. R. Grau, S. Pai, Unravelling mysteries at the
719 perivascular space: a new rationale for cerebral malaria pathogenesis. *Trends in*
720 *Parasitology* **40**, 28–44 (2024).

721 10. H. G. Augustin, G. Young Koh, G. Thurston, K. Alitalo, Control of vascular
722 morphogenesis and homeostasis through the angiopoietin–Tie system. *Nat Rev Mol Cell*
723 *Biol* **10**, 165–177 (2009).

724 11. S. Fukuhara, K. Sako, T. Minami, K. Noda, H. Z. Kim, T. Kodama, M. Shibuya, N.
725 Takakura, G. Y. Koh, N. Mochizuki, Differential function of Tie2 at cell–cell contacts and
726 cell–substratum contacts regulated by angiopoietin-1. *Nat Cell Biol* **10**, 513–526 (2008).

727 12. P. Saharinen, L. Eklund, J. Miettinen, R. Wirkkala, A. Anisimov, M. Winderlich, A.
728 Nottebaum, D. Vestweber, U. Deutsch, G. Y. Koh, B. R. Olsen, K. Alitalo, Angiopoietins
729 assemble distinct Tie2 signalling complexes in endothelial cell–cell and cell–matrix
730 contacts. *Nat Cell Biol* **10**, 527–537 (2008).

731 13. M. R. Siddiqui, C. S. Mayanil, K. S. Kim, T. Tomita, Angiopoietin-1 Regulates Brain
732 Endothelial Permeability through PTPN-2 Mediated Tyrosine Dephosphorylation of
733 Occludin. *PLOS ONE* **10**, e0130857 (2015).

734 14. P. C. Maisonpierre, C. Suri, P. F. Jones, S. Bartunkova, S. J. Wiegand, C. Radziejewski, D.
735 Compton, J. McClain, T. H. Aldrich, N. Papadopoulos, T. J. Daly, S. Davis, T. N. Sato, G.
736 D. Yancopoulos, Angiopoietin-2, a Natural Antagonist for Tie2 That Disrupts in vivo
737 Angiogenesis. *Science* **277**, 55–60 (1997).

738 15. S. Gurnik, K. Devraj, J. Macas, M. Yamaji, J. Starke, A. Scholz, K. Sommer, M. Di
739 Tacchio, R. Vutukuri, H. Beck, M. Mittelbronn, C. Foerch, W. Pfeilschifter, S. Liebner, K.
740 G. Peters, K. H. Plate, Y. Reiss, Angiopoietin-2-induced blood–brain barrier compromise
741 and increased stroke size are rescued by VE-PTP-dependent restoration of Tie2 signaling.
742 *Acta Neuropathol* **131**, 753–773 (2016).

743 16. J. Golledge, P. Clancy, J. Maguire, L. Lincz, S. Koblar, M. McEvoy, J. Attia, C. Levi, J.
744 Sturm, O. P. Almeida, B. B. Yeap, L. Flicker, P. E. Norman, G. J. Hankey, Plasma
745 Angiopoietin-1 Is Lower After Ischemic Stroke and Associated With Major Disability But
746 Not Stroke Incidence. *Stroke* **45**, 1064–1068 (2014).

747 17. T. W. Yeo, D. A. Lampah, R. Gitawati, E. Tjitra, E. Kenangalem, K. Piera, R. N. Price, S.
748 B. Duffull, D. S. Celermajer, N. M. Anstey, Angiopoietin-2 is associated with decreased
749 endothelial nitric oxide and poor clinical outcome in severe falciparum malaria.
750 *Proceedings of the National Academy of Sciences* **105**, 17097–17102 (2008).

751 18. F. E. Lovegrove, N. Tangpukdee, R. O. Opoka, E. I. Lafferty, N. Rajwans, M. Hawkes, S.
752 Krudsood, S. Looareesuwan, C. C. John, W. C. Liles, K. C. Kain, Serum Angiopoietin-1
753 and -2 Levels Discriminate Cerebral Malaria from Uncomplicated Malaria and Predict
754 Clinical Outcome in African Children. *PLOS ONE* **4**, e4912 (2009).

755 19. A. L. Conroy, E. I. Lafferty, F. E. Lovegrove, S. Krudsood, N. Tangpukdee, W. C. Liles,
756 K. C. Kain, Whole blood angiopoietin-1 and -2 levels discriminate cerebral and severe
757 (non-cerebral) malaria from uncomplicated malaria. *Malaria Journal* **8**, 295 (2009).

758 20. A. L. Conroy, S. J. Glover, M. Hawkes, L. K. Erdman, K. B. Seydel, T. E. Taylor, M. E.
759 Molyneux, K. C. Kain, Angiopoietin-2 levels are associated with retinopathy and predict
760 mortality in Malawian children with cerebral malaria: A retrospective case–control study*.
761 *Critical Care Medicine* **40**, 952 (2012).

762 21. V. Jain, N. W. Lucchi, N. O. Wilson, A. J. Blackstock, A. C. Nagpal, P. K. Joel, M. P.
763 Singh, V. Udhayakumar, J. K. Stiles, N. Singh, Plasma levels of angiopoietin-1 and -2
764 predict cerebral malaria outcome in Central India. *Malar J* **10**, 383 (2011).

765 22. C. Gomes, R. Varo, M. Duran-Frigola, A. Sitoe, R. Bila, S. Machevo, A. Mayor, Q. Bassat,
766 A. Rodriguez, Endothelial transcriptomic analysis identifies biomarkers of severe and
767 cerebral malaria. *JCI Insight* **8** (2023).

768 23. U. Fiedler, M. Scharpfenecker, S. Koidl, A. Hegen, V. Grunow, J. M. Schmidt, W. Kriz, G.
769 Thurston, H. G. Augustin, The Tie-2 ligand Angiopoietin-2 is stored in and rapidly released
770 upon stimulation from endothelial cell Weibel-Palade bodies. *Blood* **103**, 4150–4156
771 (2004).

772 24. S. Ornelas, A.-A. Berthiaume, S. K. Bonney, V. Coelho-Santos, R. G. Underly, A. Kremer,
773 C. J. Guérin, S. Lippens, A. Y. Shih, Three-dimensional ultrastructure of the brain pericyte-
774 endothelial interface. *J Cereb Blood Flow Metab* **41**, 2185–2200 (2021).

775 25. R. Daneman, A. Prat, The Blood–Brain Barrier. *Cold Spring Harb Perspect Biol* **7**,
776 a020412 (2015).

777 26. F. Fernández-Klett, J. R. Potas, D. Hilpert, K. Blazej, J. Radke, J. Huck, O. Engel, W.
778 Stenzel, G. Genové, J. Priller, Early Loss of Pericytes and Perivascular Stromal Cell-
779 Induced Scar Formation after Stroke. *J Cereb Blood Flow Metab* **33**, 428–439 (2013).

780 27. J. D. Sengillo, E. A. Winkler, C. T. Walker, J. S. Sullivan, M. Johnson, B. V. Zlokovic,
781 Deficiency in Mural Vascular Cells Coincides with Blood–Brain Barrier Disruption in
782 Alzheimer's Disease. *Brain Pathology* **23**, 303–310 (2013).

783 28. A. P. Sagare, R. D. Bell, Z. Zhao, Q. Ma, E. A. Winkler, A. Ramanathan, B. V. Zlokovic,
784 Pericyte loss influences Alzheimer-like neurodegeneration in mice. *Nat Commun* **4**, 2932
785 (2013).

786 29. V. Barrera, I. J. C. MacCormick, G. Czanner, P. S. Hiscott, V. A. White, A. G. Craig, N. A.
787 V. Beare, L. H. Culshaw, Y. Zheng, S. C. Biddolph, D. A. Milner, S. Kamiza, M. E.
788 Molyneux, T. E. Taylor, S. P. Harding, Neurovascular sequestration in paediatric P.
789 falciparum malaria is visible clinically in the retina. *eLife* **7**, e32208 (2018).

790 30. K. Haase, M. R. Gillrie, C. Hajal, R. D. Kamm, Pericytes Contribute to Dysfunction in a
791 Human 3D Model of Placental Microvasculature through VEGF-Ang-Tie2 Signaling.
792 *Advanced Science* **6**, 1900878 (2019).

793 31. M. Bernabeu, C. Gunnarsson, M. Vishnyakova, C. C. Howard, R. J. Nagao, M. Avril, T. E.
794 Taylor, K. B. Seydel, Y. Zheng, J. D. Smith, Binding Heterogeneity of Plasmodium
795 falciparum to Engineered 3D Brain Microvessels Is Mediated by EPCR and ICAM-1. *mBio*
796 **10**, e00420-19 (2019).

797 32. C. Howard, F. Joof, R. Hu, J. D. Smith, Y. Zheng, Probing cerebral malaria inflammation
798 in 3D human brain microvessels. *Cell Reports* **42**, 113253 (2023).

799 33. Y. Zheng, J. Chen, M. Craven, N. W. Choi, S. Totorica, A. Diaz-Santana, P. Kermani, B.
800 Hempstead, C. Fischbach-Teschl, J. A. López, A. D. Stroock, In vitro microvessels for the
801 study of angiogenesis and thrombosis. *Proceedings of the National Academy of Sciences*
802 **109**, 9342–9347 (2012).

803 34. T. M. Mathiisen, K. P. Lehre, N. C. Danbolt, O. P. Ottersen, The perivascular astroglial
804 sheath provides a complete covering of the brain microvessels: An electron microscopic 3D
805 reconstruction. *Glia* **58**, 1094–1103 (2010).

806 35. M. T. Uemura, T. Maki, M. Ihara, V. M. Y. Lee, J. Q. Trojanowski, Brain Microvascular
807 Pericytes in Vascular Cognitive Impairment and Dementia. *Front. Aging Neurosci.* **12**
808 (2020).

809 36. L. He, M. Vanlandewijck, E. Raschperger, M. Andaloussi Mäe, B. Jung, T. Lebouvier, K.
810 Ando, J. Hofmann, A. Keller, C. Betsholtz, Analysis of the brain mural cell transcriptome.
811 *Sci Rep* **6**, 35108 (2016).

812 37. D. Attwell, A. Mishra, C. N. Hall, F. M. O'Farrell, T. Dalkara, What is a pericyte? *J Cereb*
813 *Blood Flow Metab* **36**, 451–455 (2016).

814 38. F. Oliveira, O. Bondareva, J. R. Rodríguez-Aguilera, B. N. Sheikh, Cultured brain
815 pericytes adopt an immature phenotype and require endothelial cells for expression of
816 canonical markers and ECM genes. *Front. Cell. Neurosci.* **17** (2023).

817 39. W. Denk, H. Horstmann, Serial Block-Face Scanning Electron Microscopy to Reconstruct
818 Three-Dimensional Tissue Nanostructure. *PLOS Biology* **2**, e329 (2004).

819 40. C. J. Peddie, C. Genoud, A. Kreshuk, K. Meechan, K. D. Micheva, K. Narayan, C. Pape, R.
820 G. Parton, N. L. Schieber, Y. Schwab, B. Titze, P. Verkade, A. Aubrey, L. M. Collinson,
821 Volume electron microscopy. *Nat Rev Methods Primers* **2**, 51 (2022).

822 41. P. C. Nahirney, P. Reeson, C. E. Brown, Ultrastructural analysis of blood–brain barrier
823 breakdown in the peri-infarct zone in young adult and aged mice. *J Cereb Blood Flow*
824 *Metab* **36**, 413–425 (2016).

825 42. L. C. D. Smyth, J. Rustenhoven, E. L. Scotter, P. Schweder, R. L. M. Faull, T. I. H. Park,
826 M. Dragunow, Markers for human brain pericytes and smooth muscle cells. *Journal of*
827 *Chemical Neuroanatomy* **92**, 48–60 (2018).

828 43. R. I. Grant, D. A. Hartmann, R. G. Underly, A.-A. Berthiaume, N. R. Bhat, A. Y. Shih,
829 Organizational hierarchy and structural diversity of microvascular pericytes in adult mouse
830 cortex. *J Cereb Blood Flow Metab* **39**, 411–425 (2019).

831 44. M. R. Gillrie, G. Krishnegowda, K. Lee, A. G. Buret, S. M. Robbins, S. Looareesuwan, D.
832 C. Gowda, M. Ho, Src-family kinase–dependent disruption of endothelial barrier function
833 by Plasmodium falciparum merozoite proteins. *Blood* **110**, 3426–3435 (2007).

834 45. J. Gallego-Delgado, U. Basu-Roy, M. Ty, M. Alique, C. Fernandez-Arias, A. Movila, P.
835 Gomes, A. Weinstock, W. Xu, I. Edagha, S. C. Wassmer, T. Walther, M. Ruiz-Ortega, A.
836 Rodriguez, Angiotensin receptors and β-catenin regulate brain endothelial integrity in
837 malaria. *Journal of Clinical Investigation* **126**, 4016–4029 (2016).

838 46. P. Pal, B. P. Daniels, A. Oskman, M. S. Diamond, R. S. Klein, D. E. Goldberg,
839 Plasmodium falciparum Histidine-Rich Protein II Compromises Brain Endothelial Barriers
840 and May Promote Cerebral Malaria Pathogenesis. *mBio* **7**, 10.1128/mbio.00617-16 (2016).

841 47. J. Storm, Y. Wu, J. Davies, C. A. Moxon, A. G. Craig, Testing the effect of PAR1
842 inhibitors on Plasmodium falciparum-induced loss of endothelial cell barrier function.
843 *Wellcome Open Res* **5**, 34 (2020).

844 48. C. A. Moxon, Y. Alhamdi, J. Storm, J. M. H. Toh, D. McGuinness, J. Y. Ko, G. Murphy,
845 S. Lane, T. E. Taylor, K. B. Seydel, S. Kampondeni, M. Potchen, J. S. O'Donnell, N.
846 O'Regan, G. Wang, G. García-Cardeña, M. Molyneux, A. G. Craig, S. T. Abrams, C.-H.
847 Toh, Parasite histones are toxic to brain endothelium and link blood barrier breakdown and
848 thrombosis in cerebral malaria. *Blood Adv* **4**, 2851–2864 (2020).

849 49. S. J. Higgins, L. A. Purcell, K. L. Silver, V. Tran, V. Crowley, M. Hawkes, A. L. Conroy,
850 R. O. Opoka, J. G. Hay, S. E. Quaggin, G. Thurston, W. C. Liles, K. C. Kain,
851 Dysregulation of angiopoietin-1 plays a mechanistic role in the pathogenesis of cerebral
852 malaria. *Sci Transl Med* **8**, 358ra128 (2016).

853 50. V. Tran, A. M. Weckman, V. M. Crowley, L. S. Cahill, K. Zhong, A. Cabrera, R. E.
854 Elphinstone, V. Pearce, M. Madanitsa, L. Kalilani-Phiri, V. Mwapasa, C. Khairallah, A. L.
855 Conroy, F. O. ter Kuile, J. G. Sled, K. C. Kain, The Angiopoietin-Tie2 axis contributes to
856 placental vascular disruption and adverse birth outcomes in malaria in pregnancy.
857 *eBioMedicine* **73** (2021).

858 51. M. Zuniga, C. Gomes, Z. Chen, C. Martinez, J. C. Devlin, P. Loke, A. Rodriguez,
859 Plasmodium falciparum and TNF-α Differentially Regulate Inflammatory and Barrier
860 Integrity Pathways in Human Brain Endothelial Cells. *mBio* **13**, e01746-22 (2022).

861 52. A. Armulik, G. Genové, M. Mäe, M. H. Nisancioglu, E. Wallgard, C. Niaudet, L. He, J.
862 Norlin, P. Lindblom, K. Strittmatter, B. R. Johansson, C. Betsholtz, Pericytes regulate the
863 blood–brain barrier. *Nature* **468**, 557–561 (2010).

864 53. E. Pongponratn, G. D. H. Turner, N. P. J. Day, N. H. Phu, J. A. Simpson, K. Stepniewska,
865 N. T. H. Mai, P. Viriyavejakul, S. Looareesuwan, T. T. Hien, D. J. P. Ferguson, N. J.
866 White, An ultrastructural study of the brain in fatal Plasmodium falciparum malaria. *Am J*
867 *Trop Med Hyg* **69**, 345–359 (2003).

868 54. G. M. de Jong, J. J. Slager, A. Verbon, J. J. van Hellemond, P. J. J. van Genderen,
869 Systematic review of the role of angiopoietin-1 and angiopoietin-2 in Plasmodium species
870 infections: biomarkers or therapeutic targets? *Malaria Journal* **15**, 581 (2016).

871 55. A. L. Conroy, H. Phiri, M. Hawkes, S. Glover, M. Mallewa, K. B. Seydel, T. E. Taylor, M.
872 E. Molyneux, K. C. Kain, Endothelium-Based Biomarkers Are Associated with Cerebral
873 Malaria in Malawian Children: A Retrospective Case-Control Study. *PLOS ONE* **5**, e15291
874 (2010).

875 56. R. L. Nachman, S. Rafii, Platelets, Petechiae, and Preservation of the Vascular Wall. *New*
876 *England Journal of Medicine* **359**, 1261–1270 (2008).

877 57. P. Saharinen, L. Eklund, K. Alitalo, Therapeutic targeting of the angiopoietin-TIE pathway.
878 *Nat Rev Drug Discov* **16**, 635–661 (2017).

879 58. J. Hanson, S. J. Lee, M. A. Hossain, N. M. Anstey, P. Charunwatthana, R. J. Maude, H. W.
880 F. Kingston, S. K. Mishra, S. Mohanty, K. Plewes, K. Piera, M. U. Hassan, A. Ghose, M.
881 A. Faiz, N. J. White, N. P. J. Day, A. M. Dondorp, Microvascular obstruction and

882 endothelial activation are independently associated with the clinical manifestations of
883 severe falciparum malaria in adults: an observational study. *BMC Medicine* **13**, 122 (2015).

884 59. P. Prapansilp, I. Medana, N. T. H. Mai, N. P. Day, N. H. Phu, T. W. Yeo, T. T. Hien, N. J.
885 White, N. M. Anstey, G. D. Turner, A clinicopathological correlation of the expression of
886 the angiopoietin-Tie-2 receptor pathway in the brain of adults with Plasmodium falciparum
887 malaria. *Malaria Journal* **12**, 50 (2013).

888 60. P. Pichiule, J. C. Chavez, J. C. LaManna, Hypoxic Regulation of Angiopoietin-2
889 Expression in Endothelial Cells*. *Journal of Biological Chemistry* **279**, 12171–12180
890 (2004).

891 61. C. Sundberg, M. Kowanetz, L. F. Brown, M. Detmar, H. F. Dvorak, Stable Expression of
892 Angiopoietin-1 and Other Markers by Cultured Pericytes: Phenotypic Similarities to a
893 Subpopulation of Cells in Maturing Vessels During Later Stages of Angiogenesis *In Vivo*.
894 *Laboratory Investigation* **82**, 387–401 (2002).

895 62. T. Nishishita, P. C. Lin, Angiopoietin 1, PDGF-B, and TGF-β gene regulation in
896 endothelial cell and smooth muscle cell interaction. *Journal of Cellular Biochemistry* **91**,
897 584–593 (2004).

898 63. X. Wei, S. Jessa, C. L. Kleinman, T. N. Phoenix, Mapping Angiopoietin1 Expression in the
899 Developing and Adult Brain. *Developmental Neuroscience* **43**, 321–334 (2021).

900 64. L. Piatti, C. C. Howard, Y. Zheng, M. Bernabeu, "Binding of Plasmodium falciparum-
901 Infected Red Blood Cells to Engineered 3D Microvessels" in *Malaria Immunology*, A. T.
902 R. Jensen, L. Hviid, Eds. (Springer US, New York, NY, 2022;
903 https://link.springer.com/10.1007/978-1-0716-2189-9_43)vol. 2470 of *Methods in*
904 *Molecular Biology*, pp. 557–585.

905 65. B. Titze, C. Genoud, R. W. Friedrich, SBEMimage: Versatile Acquisition Control Software
906 for Serial Block-Face Electron Microscopy. *Front. Neural Circuits* **12** (2018).

907 66. G. Mahalingam, R. Torres, D. Kapner, E. T. Trautman, T. Fliss, S. Seshamani, E. Perlman,
908 R. Young, S. Kinn, J. Buchanan, M. M. Takeno, W. Yin, D. J. Bumbarger, R. P. Gwinn, J.
909 Nyhus, E. Lein, S. J. Smith, R. C. Reid, K. A. Khairy, S. Saalfeld, F. Collman, N. Macarico
910 da Costa, A scalable and modular automated pipeline for stitching of large electron
911 microscopy datasets. *eLife* **11**, e76534 (2022).

912 67. waleedmirzaPhD, waleedmirzaPhD/cell_analysis_toolkit, (2024);
913 https://github.com/waleedmirzaPhD/cell_analysis_toolkit.

914 68. P. Virtanen, R. Gommers, T. E. Oliphant, M. Haberland, T. Reddy, D. Cournapeau, E.
915 Burovski, P. Peterson, W. Weckesser, J. Bright, S. J. van der Walt, M. Brett, J. Wilson, K.
916 J. Millman, N. Mayorov, A. R. J. Nelson, E. Jones, R. Kern, E. Larson, C. J. Carey, İ.
917 Polat, Y. Feng, E. W. Moore, J. VanderPlas, D. Laxalde, J. Perktold, R. Cimrman, I.
918 Henriksen, E. A. Quintero, C. R. Harris, A. M. Archibald, A. H. Ribeiro, F. Pedregosa, P.
919 van Mulbregt, SciPy 1.0: fundamental algorithms for scientific computing in Python. *Nat*
920 *Methods* **17**, 261–272 (2020).

921

Fig. S1.

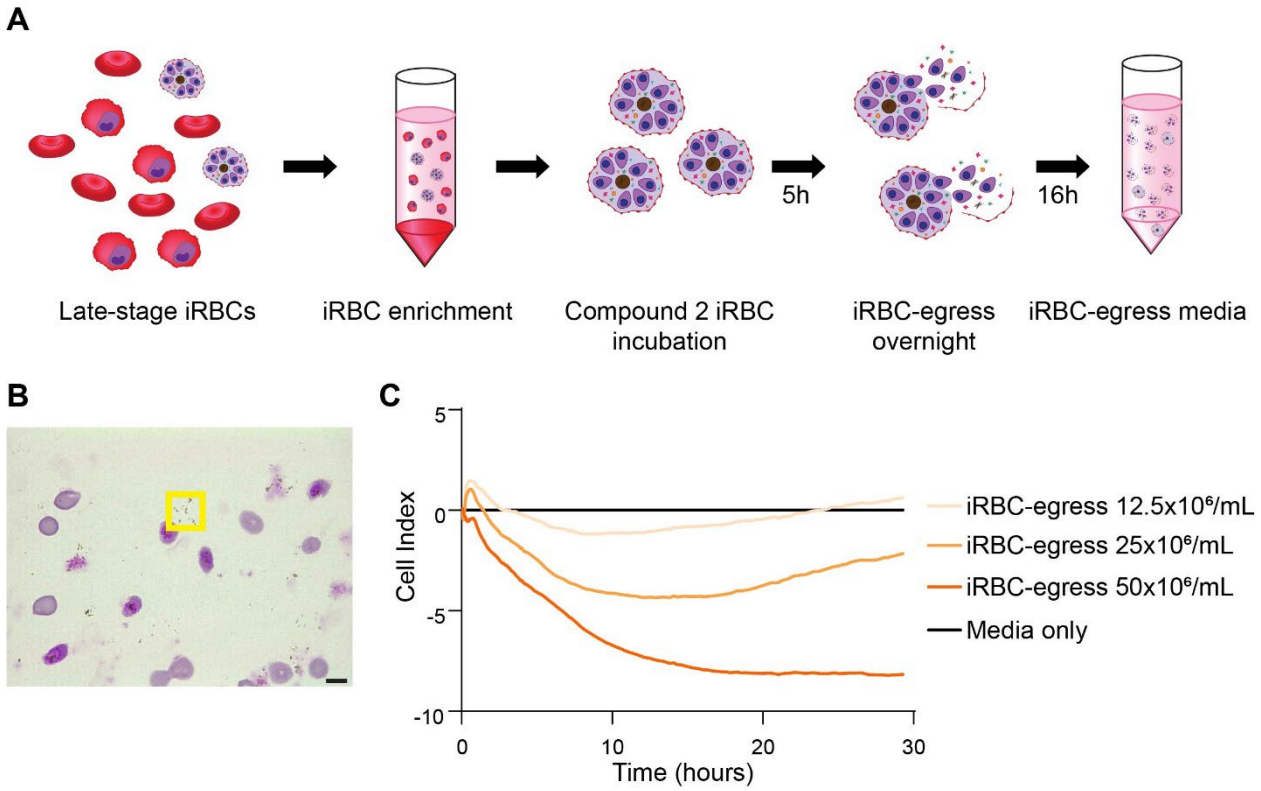

Fig. S1. Preparation of iRBC-egress media that induces barrier breakdown. (**A**) Schematic representation of the protocol to make iRBC-egress media. In short, late-stage *P. falciparum*-iRBC are purified by a gelaspan gradient separation and then incubated for 5 hours with compound-2 to synchronize them at the point of egress. Compound-2 is removed and the *P. falciparum*-iRBC are resuspended in vascular growth media and left overnight on a shaker at 50 rpm to egress. (**B**) A thin smear taken from the resultant iRBC-egress media before centrifugation stained with giemsa. The yellow box highlights free hemozoin particles. Scale bar represents 5 µm. (**C**) Representative recording data of xCELLigence measurements on 2D HBMEC monolayers in the absence of HBVP taken after addition of iRBC-egress media at different concentrations. Data is normalized to the media-only control.

Fig. S2.

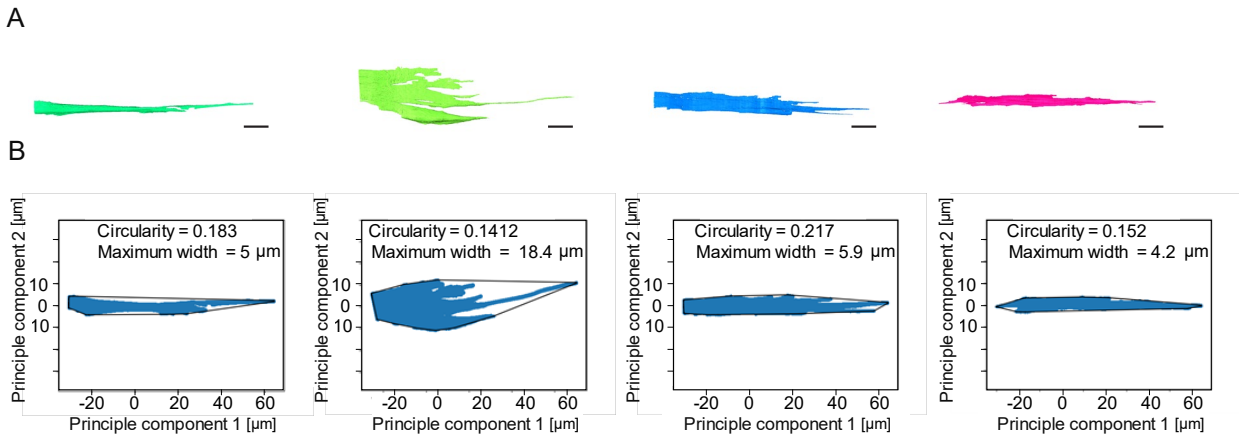

Fig. S2. Morphology analysis of segmented pericytes from SBF-SEM. (**A**) The analysis pipeline begins with the extraction of 3D segmented pericyte meshes. Shown here are four representative pericytes. (**B**) Pericyte geometry is flattened into two principal dimensions using PCA by a Python-based image analysis pipeline. The 2D geometry's shape is then determined using convex hull analysis. To describe pericyte morphology, pericyte cell borders are analyzed for circularity, calculated as 4π*Area/Perimeter^2, where a value of 1 indicates a perfect circle and values approaching 0 indicate increasingly elongated shapes, and maximum width.

Fig. S3.

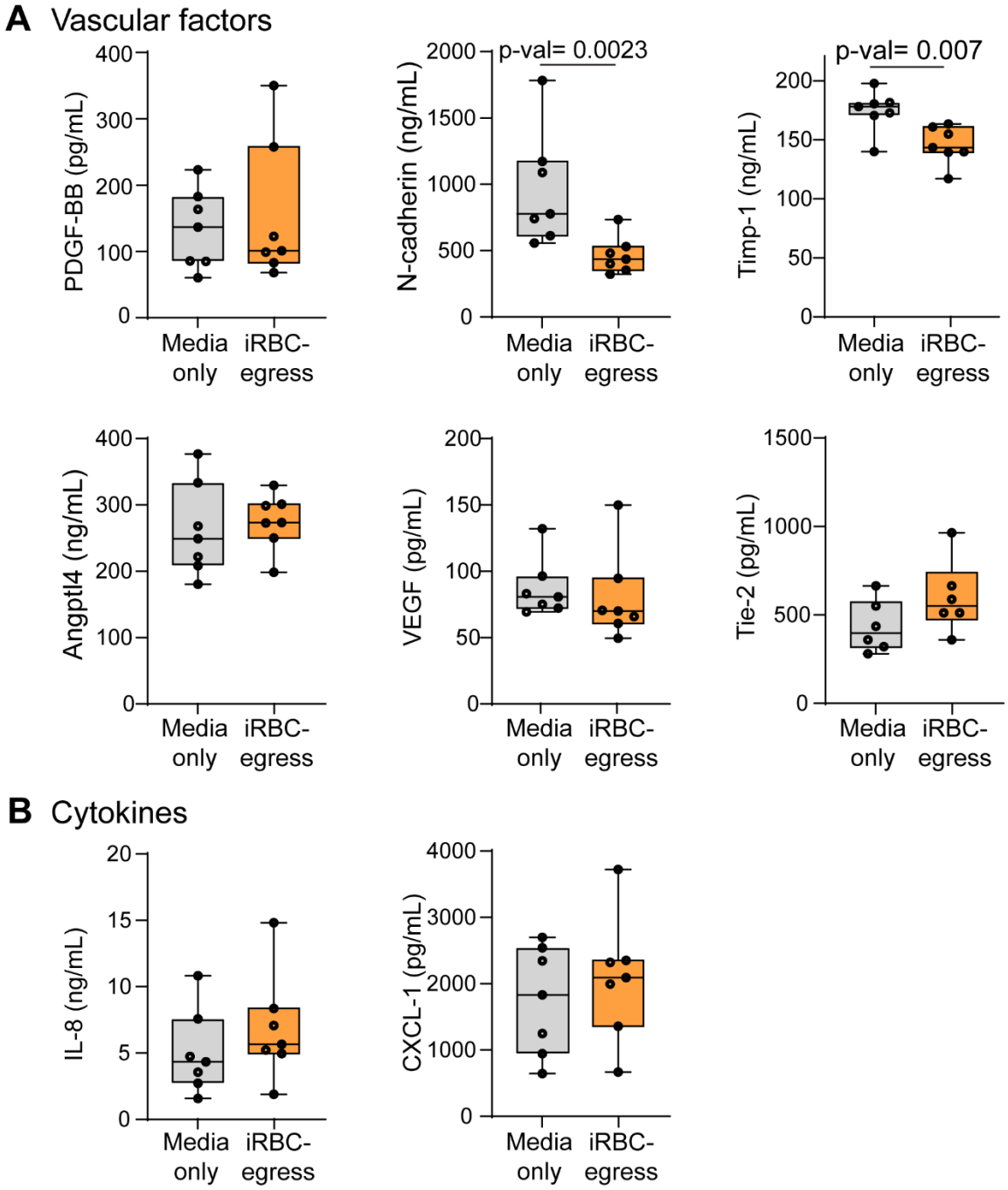

Fig. S3. Changes in secreted vascular factors and cytokines following iRBC-egress media incubation. (**A**) Concentrations of vascular factors PDGF-BB, N-cadherin, Timp-1, Angptl4, VEGF and Tie-2 measured by Luminex from 3D brain microvessels supernatants treated with media only or iRBC-egress media for 18-hours. (**B**) Concentrations of released cytokines IL-8 and CXCL-1 measured by Luminex from 3D brain microvessels supernatants treated with media only or iRBC-egress media for 18-hours. Box and whisker plots display the median, 25th and 75th percentiles and the minimum and maximum data points in A and B. Data points represent supernatants pooled from 2-3 devices in 6-7 independent experiments. Statistical significance is analyzed by Mann-Whitney U test.

Fig. S4.

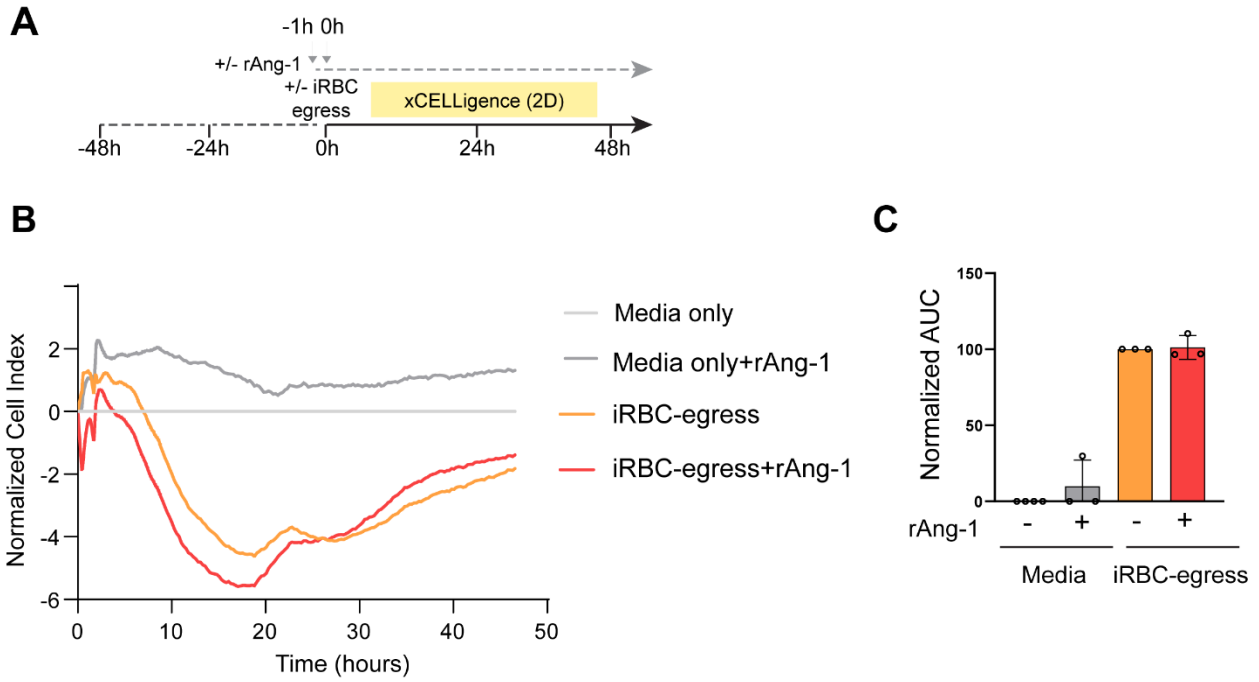

Fig. S4. Short time pre-incubations with rAng-1 does not protect against increased permeability induced by iRBC-egress media. (**A**) Experimental outline of short-term (1-hour) incubation with rAng-1 in a 2D HBMEC monolayer in the absence of HBVP. (**B**) Representative recording data of xCELLigence measurements taken after +/- addition of rAng-1 followed by addition of media only or iRBC-egress media. All conditions were normalized to the media only control. (**C**) Area under the curve analysis. All conditions were normalized to *P. falciparum*-iRBC-egress media as 100. Data points represent 3 independent experiments run in triplicate. Statistical significance is analyzed by repeated measures one-way ANOVA test with Dunnett's multiple comparisons test.